

Master Thesis



Czech
Technical
University
in Prague

F4

Faculty of Nuclear Sciences and Physical Engineering
Department of Solid State Engineering

Laser-Ultrasonic Characterization of NiTi Thin Films

Zuzana Soudná

Supervisor: Ing. Tomáš Grabec, PhD.
Supervisor–specialist: Ing. Pavla Stoklasová, PhD.
January 2023



ČESKÉ VYSOKÉ UČENÍ TECHNICKÉ V PRAZE
FAKULTA JADERNÁ A FYZIKÁLNĚ INŽENÝRSKÁ
Katedra inženýrství pevných látek

ZADÁNÍ DIPLOMOVÉ PRÁCE

Student: Bc. Zuzana Soudná

Studijní program: Inženýrství pevných látek

Akademický rok: 2021/2022

Název práce: Charakterizace tenkých vrstev slitiny NiTi pomocí laserově
(česky) ultrazvukových metod

Název práce: Laser-Ultrasonic Characterization of NiTi thin films
(anglicky)

Pokyny pro vypracování:

Diplomová práce bude zaměřena na určení elastických vlastností vzorků řádově mikrometricky tenkých vrstev slitiny NiTi, které byly připraveny epitaxním růstem na substrátu MgO na pracovišti IFW v Drážďanech. Jejich charakterizace bude probíhat na základě výsledků experimentálních měření frekvenční a úhlové disperze rychlosti povrchových akustických vln pomocí dvou laserově ultrazvukových metod, a to tzv. spektroskopie s přechodovou mřížkou (*transient grating spectroscopy – TGS*) a povrchové Brillouinovy spektroskopie (*surface Brillouin spectroscopy – SBS*). Cílem práce bude seznámit se s oběma jmenovanými experimentálními metodami a využít je pro určení rychlosti povrchových vln, a následně ze získaných dat vyhodnotit vlastnosti vrstev pomocí numerických metod.

Experimentální část práce proběhne na Oddělení ultrazvukových metod Ústavu termomechaniky AV ČR.

Při řešení postupujte podle následujících bodů.

I. Rešeršní/teoretická část

- 1) Seznamte se s teorií šíření povrchových akustických vln v tenkých vrstvách na substrátech, vazbou mezi frekvenční a úhlovou disperzí jejich rychlosti a s elastickými parametry tenkých vrstev.
- 2) Seznamte se s principy laserově ultrazvukových experimentálních metod měření povrchových elastických vln, zejména pak s metodami spektroskopie s přechodovou mřížkou (TGS) a povrchové Brillouinovy spektroskopie (SBS) a s jejich realizací na Ústavu termomechaniky AV ČR.
- 3) Seznamte se s principem určení elastických parametrů tenkých vrstev z měření povrchových vln pomocí numerické inverzní metody.

II. Experimentální část

- 1) Proved'te sadu měření pomocí laserově ultrazvukových metod TGS a SBS pro vzorky tenkých epitaxních vrstev NiTi na substrátu MgO.
- 2) Zpracujte získaná experimentální data a diskutujte možnost určení frekvenční disperze povrchových vln ve frekvenčním pásmu stovek megahertzů až jednotek gigahertzů.
- 3) Na základě vyhodnocených dat diskutujte možnosti charakterizace měřených vzorků především z hlediska určení elasticity a tloušťky měřených vrstev.

Doporučená literatura:

- [1] P. Stoklasová, T. Grabec, K. Zoubková, P. Sedlák, H. Seiner: Laser-Ultrasonic Characterization of Strongly Anisotropic Materials by Transient Grating Spectroscopy. *Experimental mechanics* 61(4) (2021) 663–676.
- [2] G. Carlotti: Elastic Characterization of Transparent and Opaque Films, Multilayers and Acoustic Resonators by Surface Brillouin Scattering: A Review. *Applied Sciences* 8(1) (2018) article #124.
- [3] P. Stoklasová, P. Sedlák, H. Seiner, M. Landa: Forward and Inverse Problems for Surface Acoustic Waves in Anisotropic Media: a Ritz-Rayleigh method based approach. *Ultrasonics* 56 (2015) 381–389.
- [4] A.G. Every, A.A. Mazev, W. Grill, M. Pluta, J.D. Comins, O.B. Wright, O. Matsuda, W. Sachse, J.P. Wolfe: Bulk and surface acoustic wave phenomena in crystals: Observation and interpretation. *Wave Motion* 50(8) (2012) 1197–1217.

Jméno a pracoviště vedoucího práce:

Ing. Tomáš Grabec, Ph.D., Katedra inženýrství pevných látek Fakulta jaderná a fyzikálně inženýrská, ČVUT v Praze.

Jméno a pracoviště konzultanta:

Ing. Pavla Stoklasová, Ph.D., Ústav termomechaniky AV ČR, v.v.i.

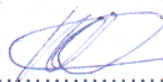
Datum zadání diplomové práce: 21. 10. 2021

Termín odevzdání diplomové práce: 5. 5. 2022

Doba platnosti zadání je dva roky od data zadání.



garant



vedoucí katedry



děkan

V Praze dne 21. 10. 2021

Acknowledgements

Tomáš Grabec

D 5 - Ultrasonic Methods

Pavla Stoklasová

Kristýna Zoubková

Martin Ševčík

Family

Alena Krechlerová

Zuzana Soudná

Dedicated to my grandmother, who provided me with a roof over my head, an ever-full belly, and never-ending care for my grades during my master's studies.

And to my dad, who for the last three decades has supported me in anything I could think of, including studying extra-long at his expense. Thanks for sticking it out until "the finals". And dad, keep strong, PhD #1 is around the corner, I'm not even halfway through! ;)

This work was supported by the Grant Agency of the Czech Technical University in Prague, grant No. SGS22/183/OHK4/3T/14.

Declaration

I hereby declare that I have written this work completely by myself and that I have cited all used sources in the bibliography.

Prague, January 5, 2023

Abstract

The thesis is dedicated to characterization of epitaxial NiTi thin films by non-contact transient grating spectroscopy which excites and detects surface acoustic waves propagating in the media. In situ measurement during thermal cycling confirmed the properties of the martensitic phase transition and the transformation temperatures of the epitaxial film, and suggested a presence of R-phase. Angular dispersion provided input data for Ritz-Rayleigh numerical method for calculation of elastic constants, showing that the epitaxial film is more anisotropic in the martensitic phase, even though it forms a complex microstructure of martensitic variants, compared to the single-crystalline austenite. Also, it was demonstrated that the film thickness to wavelength ratio plays a key role in extracting maximal available information about the measured sample since it directly affects the number of wave modes propagating in the film and consequent success of the Ritz-Rayleigh inversion.

Keywords: epitaxial thin films, NiTi, surface acoustic waves, transient grating spectroscopy, Ritz-Rayleigh numerical method

Supervisor: Ing. Tomáš Grabec, PhD.
Department of Solid State Engineering,
Faculty of Nuclear Sciences and Physical
Engineering,
Czech Technical University in Prague

Abstrakt

Diplomová práce se věnuje charakterizaci epitaxních tenkých vrstev NiTi bezkontaktní spektroskopií s přechodovou mřížkou, která excituje a detekuje povrchové akustické vlny šířící se prostředím. In situ měření během teplotního cyklování potvrdilo vlastnosti martenzitického fázového přechodu a transformační teploty epitaxní vrstvy, a naznačilo přítomnost R-fáze. Úhlová disperze poskytla vstupní data pro Ritzovu-Rayleighovu numerickou metodu pro výpočet elastických konstant, ukazujících na vyšší anizotropii epitaxní vrstvy v martenzitické fázi, navzdory tvorbě komplexní mikrostruktury martenzitických variant, v porovnání s monokrystalickým austenitem. Také bylo ukázáno, že poměr tloušťky vrstvy a vlnové délky hraje klíčovou roli ve vytěžení maxima možných informací o měřeném vzorku, jelikož přímo ovlivňuje počet vlnových módů šířících se vrstvou a následný úspěch Ritzovy-Rayleighovy inverze.

Klíčová slova: epitaxní tenké vrstvy, NiTi, povrchové akustické vlny, spektroskopie s přechodovou mřížkou, Ritzova-Rayleighova numerická metoda

Překlad názvu: Charakterizace tenkých vrstev slitiny NiTi pomocí laserově ultrazvukových metod

Contents

1 Introduction	1	7 Conclusion	46
2 Shape-memory effect	2	Bibliography	48
2.1 Thermoelastic martensitic transformation	3		
2.1.1 Austenite and martensite	3		
2.1.2 Macroscopic perspective: hysteresis	4		
2.1.3 Microscopic perspective: lattice deformation and accommodation	5		
2.1.4 Summary: martensitic transformation supporting shape memory effect	7		
2.2 Superelasticity and pseudoplasticity	7		
2.3 NiTi	9		
2.3.1 NiTi thin films	11		
3 Wave propagation in solids	13		
3.1 Hooke's law	13		
3.1.1 Effect of crystal symmetry on the number of independent elastic constants	14		
3.2 Christoffel's equation	15		
3.2.1 Wave polarisation	16		
3.2.2 Characteristic surfaces	17		
3.3 Guided waves	19		
3.3.1 Free surface	20		
3.3.2 Plate	22		
3.3.3 Film-substrate system	23		
4 Laser-ultrasonics	26		
4.1 Photothermal generation	26		
4.2 Transient Grating Spectroscopy	27		
5 Ritz-Rayleigh numerical method	32		
5.1 Forward problem	32		
5.1.1 Calculation for the supported layer	35		
5.2 The inverse problem	36		
6 Characterization of NiTi thin films	37		
6.1 Samples	37		
6.2 TGS of thermally cycled NiTi thin film sample	39		
6.2.1 Ritz-Rayleigh calculation for the NiTi thin films	41		
6.3 TGS of NiTi thin films of various thicknesses	42		

Figures

2.1 Change in unit cell shape	4	6.4 Angular velocity maps of austenite and martensite in NiTi3100	41
2.2 Stress-strain hysteresis	5	6.5 Angular velocity maps of NiTi epitaxial thin films at room temperature	43
2.3 SME microscopically	6		
2.4 Shape accommodation by slip and twinning	6		
2.5 SME mechanism	8		
2.6 Crystal structures of austenite and martensite	10		
2.7 Crystal structure of R-phase . . .	10		
2.8 M_s dependence on Ni content . .	11		
3.1 Deformation of a crystalline lattice during a longitudinal wave propagation	16		
3.2 Propagation in an anisotropic crystal	17		
3.3 Slowness surface of a cubic system of Si	18		
3.4 Directions in a semi-infinite crystal	19		
3.5 Rayleigh wave in an isotropic semi-infinite solid	21		
3.6 TH-type surface wave	21		
3.7 Rayleigh and pseudo-Rayleigh wave propagation in a cubic crystal	22		
3.8 Lamb waves in an isotropic plate	23		
3.9 Purely TH wave in a plate	23		
3.10 Wave dispersion in slow-on-fast system	25		
3.11 Love wave	25		
4.1 Wave fronts generated by a source	27		
4.2 Photothermal generation	27		
4.3 TGS setup	28		
4.4 Littrow configuration	29		
4.5 TGS signal	30		
5.1 Computational domain of a plate	33		
5.2 Computational domain of a film-substrate system	35		
6.1 SEM of NiTi thin films	38		
6.2 Thermal velocity maps of thermally cycled NiTi3100 at $10\ \mu\text{m}$ at two various angles	39		
6.3 Thermal hysteresis of SAW velocity of NiTi3100	40		

Tables

2.1 Characteristic lattice parametres for NiTi alloys	9
3.1 Type of elastic waves	20
6.1 NiTi thin films properties	37



Chapter 1

Introduction

This thesis deals with characterization of epitaxial NiTi thin films by the means of surface acoustic waves (SAWs) excited and detected with the transient grating spectroscopy (TGS).

Since the first report in the 1960s, bulk NiTi has become arguably the most researched and famous shape-memory alloy to date, and yet, there is a significant gap in the knowledge of the unit-cell elasticity, which is necessary for better understanding and modelling of its behaviour. Unfortunately, its prolonged periods of heat transfer limit its utilization in practical applications, e.g. actuators, where a fast response to temperature change is desired. Therefore, thin shape-memory films demonstrating more distinct changes in properties during phase transformation have become the object of interest. Since 1990s, sputtered NiTi thin films were investigated, however, only effective elasticity can be determined from polycrystalline material. Since monocrystalline NiTi enabling determination of elastic constants of the unit cell is difficult to obtain, the here studied epitaxial thin films, provided by Helmholtz-Zentrum Dresden-Rossendorf, may serve as an alternative.

In the theoretical part, the general principles valid in shape-memory alloys, specific characteristics of NiTi as well as introduction to various wave types propagating in the media are described. Further are introduced the principles and set-up of TGS used to excite and detect the waves in the samples. While TGS is suitable for measurements of elastic waves with wavelengths in the order of unit to tens of micrometers (that is, frequencies typically in hundreds of MHz to low GHz), surface Brillouin spectroscopy (SBS) [1] might serve as a complimentary technique to TGS, providing information about waves with wavelengths in the order of hundreds of nanometers (frequencies in units to tens of GHz [2]). Unfortunately, SBS was omitted due to unexpected technical reasons. Nevertheless, the information obtained by TGS was sufficient to calculate elastic constants of the thickest film by the Ritz-Rayleigh numerical method.

In total, three epitaxial NiTi thin films of various thicknesses were investigated. Although angular dispersion was measured for all of them, thermal cycling and unit cell elasticity calculation were performed only for the sample with the highest thickness.

Chapter 2

Shape-memory effect

The physical key to shape-memory effect, including superelasticity, lies in a reversible phase transformation. By phase, e.g. austenite and martensite, is understood an inner arrangement of crystal structure with stable and uniform properties in a specific thermodynamical region. It was outlined that modification of the crystalline structure is caused by a change in the external environment, i.e., a change in temperature, stress, etc; thermal and mechanical stresses have reciprocal influence.

The shape-memory effect (SME) is categorised according to:

- Driving force of martensitic phase formation:
 - **Thermal:** at start temperature of martensitic transformation M_s under no stress
 - **Mechanical:** above M_s if stress is applied; see more about stress-induced martensite (SIM) in [3]
- Direction of occurrence:
 - **One-way:** the shape change caused by the SME occurring only upon heating
 - **Two-way;** for further information about the principle [3] and about the introduction of the effect in NiTi [4].

Only the thermal one-way shape-memory effect will be discussed further.

Thermal shape-memory is the ability of a material to restore its original shape after a thermal load is applied. One-way thermal shape memory indicates that after a mechanical loading unloading process at low temperature, an increase in temperature induces a spontaneous recovery of the residual strains, i.e. of the original, pre-deformation shape.

The transformation related to thermal one-way shape memory and superelasticity in crystalline metallic materials is called the thermoelastic martensitic transformation, which will be discussed further with emphasis on the phenomena taking place in the NiTi alloy as the subject of this thesis.

2.1 Thermoelastic martensitic transformation

Martensitic transformation in shape-memory alloys is a reversible solid-to-solid phase transformation between phases called austenite and martensite, see Fig. 2.1, with the following characteristics:

- **First order transformation:** releases heat during martensite formation, has a hysteresis and a temperature range over which austenite and martensite coexist
- **Athermal:** the amount of the new phase is usually dependent only upon temperature, not the amount of time subjected to the temperature
- **Displacive** (in most cases)

The displacive, i.e. diffusionless nature of martensitic transformation indicates that despite the abrupt change of the crystalline lattice parameters and significant lattice distortion at a specific temperature, the relative positions of atoms are invariable. The invariability is mediated by a well-coordinated shear dominant atomic displacement as shown in Fig. 2.1; the displacement motion between two phases is limited only by the transverse-wave velocity. The displacements are so small compared to the interatomic distance that they do not escape the original crystal. Therefore, the volume change can be very small. However, the related progress of the transformation still induces a large shear strain.

2.1.1 Austenite and martensite

The existence of two phases, one stable at low and one at high temperature, is a necessary precondition for martensitic transformation. The high-temperature phase is called the parent phase or austenite, named after English physicist Charles Austen, and typically possesses a centred cubic structure. The low-temperature phase is called the product phase, or martensite, named after the German physicist Adolf Martens. A schematic aspect of martensite and austenite crystals is reported in Fig. 2.1.

Since the martensitic phase has typically a lower degree of crystallographic symmetry than the austenitic phase, the inverse transformation from martensite to austenite runs in one specific way while there are several alternative routes to multiple symmetry-related martensite variants; see the example in Fig. 2.3b and Fig. 2.4b. This geometrical concept drives the shape-memory effect.

The number ν of variants obtained depends on the change in symmetry during the transformation:

$$\nu = \frac{\text{number of rotations in } P_a}{\text{number of rotations in } P_m}, \quad (2.1)$$

where P_a and P_m are the symmetry groups of austenite and martensite, respectively. The austenite crystal can transform into a mixture of martensite

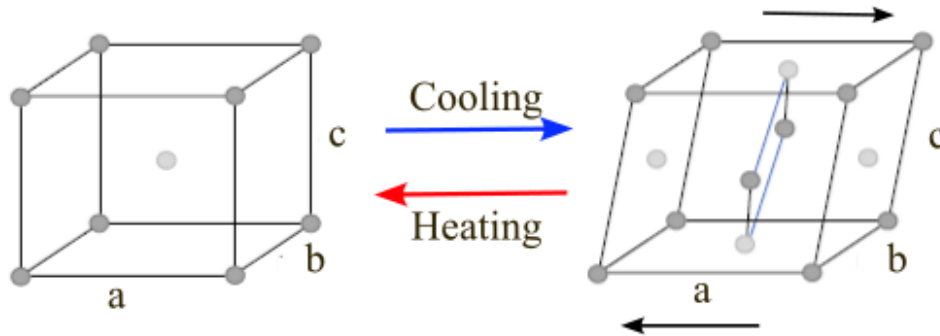


Figure 2.1: Change in unit cell shape in Nickel-Titan alloy on martensitic transformation from austenite (left) to martensite (right), where light gray dots refer to titanium atoms and dark gray dots to nickel atoms. Adapted from [5]

variants; however, since the martensitic transformation shows some special characteristics, see [6], the rows of atoms on the interface between the variants are not broken so that the whole crystal remains coherent. The various mixtures of variants, creating characteristic twin patterns, are termed the microstructure of martensite.

2.1.2 Macroscopic perspective: hysteresis

Martensitic transformation takes place within a certain temperature range, which is characterised by four transformation temperatures depending on the direction of the thermodynamic process:

- martensitic transformation start temperature M_s ,
- martensitic transformation finish temperature M_f ,
- reverse transformation start temperature A_s ,
- reverse transformation finish temperature A_f .

When the material is cooled from above A_f to below M_s , the parent phase transforms through an exothermic reaction into a low temperature phase without change in shape, see Fig. 2.3b. In the interval from M_s to M_f , the temperature drop increases the volume fraction of martensite in parent austenite until the full transformation, the composition and atomic order of the parent phase are preserved. If the material is deformed below M_f , heating up above A_s transforms the product martensitic phase via an endothermic reaction into the high-temperature phase. The shape recovery starts at A_s and ends at A_f where the initial shape is recovered. Again, no change in shape occurs when the temperature is cooled back below M_f , and deformation below M_f must occur again to reactivate shape-memory. The difference of transformation temperatures for forward and reverse transformation, see Fig. 2.2, is called transformation hysteresis. The hysteresis explains the one-way

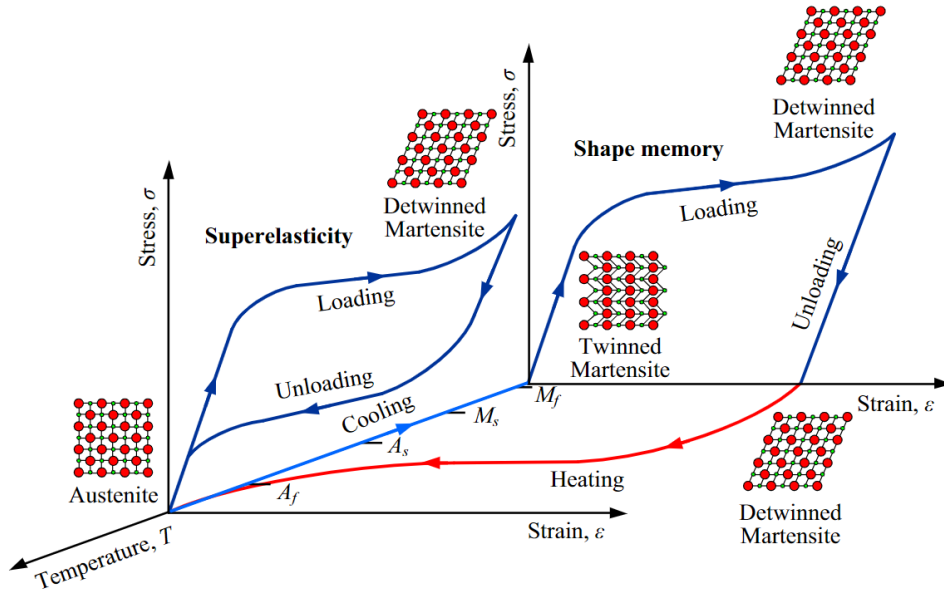


Figure 2.2: Scheme of stress–strain hysteresis for shape-memory effect and superelasticity of SMAs; taken from [7]

SME which is macroscopically viewed as a cancelation of the impressed deformation. Typical magnitude values of hysteresis for shape-memory alloys are in the small range of 20-40 °C [3] according to the alloy. The hysteresis is caused by a different mobility of the austenite/martensite interface; this microscopical explanation will be discussed further in detail.

2.1.3 Microscopic perspective: lattice deformation and accommodation

The martensitic transformation occurs in such a way that the interface between the martensite variant and parent phase becomes an undistorted and unrotated plane, i.e. invariant plane or habit plan, in order to minimise the strain energy. Crystallographically, the martensitic transformation consists of two parts: the Bain strain, i.e. lattice deformation, and the lattice-invariant shear, i.e. accommodation. For simplicity, assume a two-dimensional case from now on.

The lattice deformation comprises all the atomic movements needed for the phase transformation. Fig. 2.3 shows the progress of the structure from austenite to martensite phase. The interface progresses one atomic layer, until small coordinated movements, i.e., the Bain strain, assemble the new martensitic structure. The new martensitic structure is of different shape and often volume than the surrounding austenite, compare Fig. 2.3a and 2.3c; for NiTi, the volume change can be neglected. Therefore, either the overall shape of the new martensitic phase or the surrounding austenitic phase must be modified to accommodate the new structure.

Accommodation is the second part of the martensitic transformation which

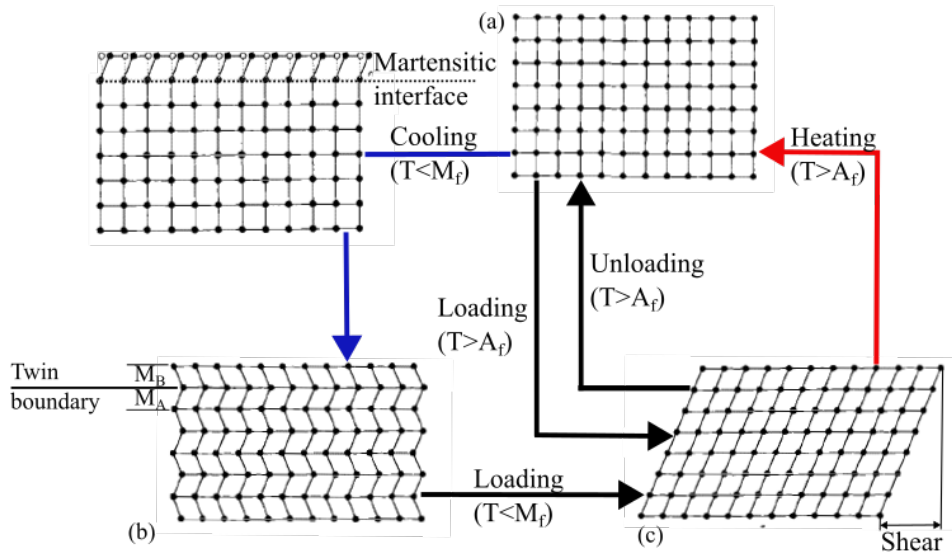


Figure 2.3: SME microscopically: cooling down austenite (a) leads to a formation of twinned martensite (b) of the same shape, deformation of (b) by moving twin boundaries leads to a change in shape. Heating of (b) or (c) leads to recovery of austenitic structure and its original shape. Taken from [3]

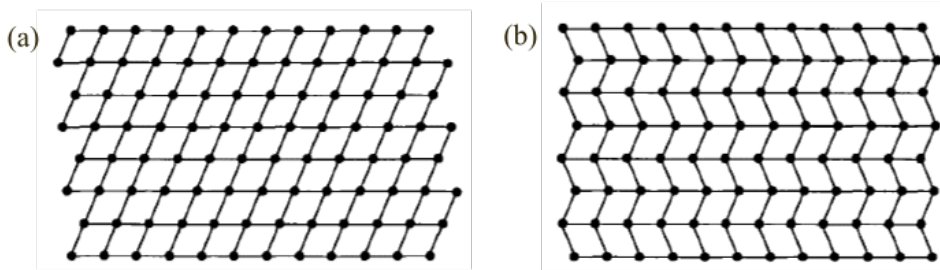


Figure 2.4: Mechanism of shape accommodation due to atomic shear of martensitic transformation: (a) slip (irreversible), (b) twinning (reversible); adapted from [3]

ensures that the new martensitic structure has the shape of the original austenite. In the two-dimensional model of Fig. 2.4, during austenite cooling (Fig. 2.3 a), two variants of shear (Fig. 2.3b) are required to comprise the new martensitic structure below M_f to restore the original overall shape of the matrix. The introduced lattice-invariant shear can occur through two mechanisms: twinning (Fig. 2.4b) and slip (Fig. 2.4a).

Twinning is a reversible shape accommodation mechanism dominant in the SMAs; it is applicable only if no volume change is involved. Contact of different martensite variants forms twin boundaries, see Fig. 2.3b . The twin boundary is a mirror plane, i.e. atoms positioned on that boundary see mirror views on both sides of the boundary. Since the atoms on the boundary are bonded in a similar way as the atoms located outside the boundary, they neighbour with the same number of atoms. Therefore, the twin boundaries

account for very low-energy interfaces, are quite mobile, and on top of that, the stability of martensitic phase is only weakly affected by the number of locations of these boundaries.

When comparing the edges of the structures in Fig. 2.4a and Fig. 2.4b, all bonds in the twinned structure remain intact. If a stress is applied to the structure shown in Fig. 2.4b, the different martensite variants in touch on the twin boundary convert mutually to each other in a process called martensite reorientation. In this way, the twin boundary moves and produces a shape that better accommodates the applied stress. This means that the shape accommodation is executed through martensite variant redistribution in such a way that the opposite shear directions, twin-related with each other, cancel out the shear deformation of the twins, and so minimise the material deformation. In the ideal case, the twin variants condense into a single favourable variant of martensite; the process is called detwinning. The reversion of a martensite is just a reversal of crystallography: it undergoes backward shear until the twinning, and at the end, the martensite itself disappears. Note that twin boundaries refer both to boundaries within martensite plates as discussed herein and to boundaries between adjoining martensite plates.

Slip, i.e. shift of atomic planes, is a common accommodation mechanism accompanying twinning in many martensites. Either it relaxes the stress induced near the twin boundary due its insufficient compatibility or it occurs as a next step during mechanical loading when the potential of twinning to accommodate the external strain is depleted. Since slip requires breaking atomic bonds, it is irreversible.

■ 2.1.4 Summary: martensitic transformation supporting shape memory effect

The mechanism of the SME is illustrated in Fig. 2.5a. At low temperatures, including room temperatures, there are SMAs in the martensitic phase, where their shape can easily be changed by twinning or detwinning. The deformation is seen as a change in the fraction of the variants. Reorientation of martensitic grains can lead to a detwinned microstructure. Heating above A_f leads to a transformation into an austenitic structure and recovery of the original shape thanks to all variants of martensites originating from a single austenite crystal. This is called a shape-memory effect. Repeated cooling below M_f leads to the transformation back to twinned martensite, however, due to self-accommodated structures without change in shape. The corresponding changes in atomic structures during the martensitic transformation are depicted in Fig. 2.5b.

■ 2.2 Superelasticity and pseudoplasticity

Response of shape-memory alloy to loading, as depicted in Fig.2.2, manifests itself on a macroscopic scale in two distinct characteristics: superelasticity

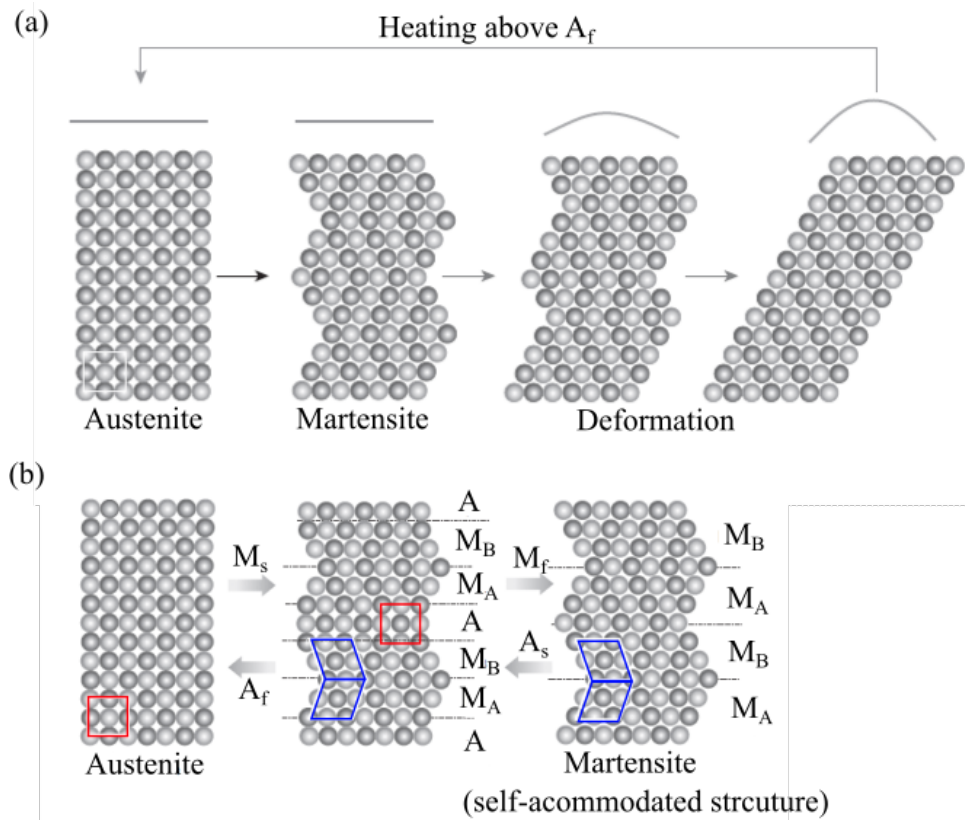


Figure 2.5: SME: (a) mechanism, (b) atomic arrangement during martensitic transformation, where A is austenitic (parental) phase, M martensitic phase, M subscripts A and B refer to martensite crystals with different shear directions. Adapted from [4]

and pseudoplasticity.

Superelasticity refers to a temperature-independent shape-memory. First, a loading of austenite induces phase transformation into so called stress-induced martensite (SIM). Further loading leads to a detwinning and change in shape of the martensite. However, the crystal rearrangement is reversible and therefore, when the martensite is unloaded, full recovery to austenite in the initial shape occurs. Superelasticity is sometimes referred to as pseudoelasticity since, unlike in case of true elasticity, the key element is not in the change of the interatomic distances in the material but rather a change of the crystal lattice type.

Pseudoplasticity refers to a temperature-dependent shape-memory. First, a loaded austenite transforms into martensite again, however this time the resulting martensite is stable and the deformed shape is preserved even when unloaded, i.e., it seems that the material has been plastically deformed. However, when the deformed martensite is heated up, it recovers the initial shape of austenite. Recovery of the initial shape of austenite by subjecting martensite to an increased temperature is referred to as the shape-memory effect. The recoverable strains of typical shape-memory alloys are of the order

of several percent [3].

2.3 NiTi

Scientific interest in shape-memory alloys was triggered by studies on NiTi alloys. The first report on SME in Ti-Ni alloy in 1963 [9]. A series of NiTi alloys was patented in the USA in 1965 by Buehler and Wiley employed at the US Naval Ordnance Laboratory (NOL). That is where the name Nitinol comes from, NiTi standing for the chemical symbols of the constituents, and NOL is the laboratory acronym. However, despite the great shape memory characteristics in general, for example having a shape memory strain of up to 8 % [10] compared to 4 - 5 % [10] of copper- and iron-based alloys, only a few commercial articles were introduced in the 1960s and 1970s; for more details of the history of NiTi development, see [5]. In 1989, SME and SE in NiTi alloys were shown [11].

Regarding other properties of NiTi alloys, they demonstrate a great response in terms of impact resistance and outstanding general structural and workability properties. However, it was the near-perfect biocompatibility, together with excellent corrosion resistance and thermal stability, that led to an outburst in the NiTi implementation. These are the characteristics required for long-term installations, inclusive biomedical applications such as orthopaedic implants and cardiovascular stents. Furthermore, NiTi is a nonferromagnetic alloy and therefore does not interfere during magnetic resonance imaging-based surgery, whether in patient implants or surgical tools. On the other hand, even though NiTi alloys are considered safe in the human body, pure Ni is toxic and causes hypersensitivity, which drives the development of Ni-free Ti-based alloys as a possible alternative for medical applications.

SMAs are generally based on a bcc symmetry and a bcc or more often a B2 structure. The ordering of NiTi atoms is depicted in Fig. 2.1 and in more detail in Fig. 2.6. Martensite adopts austenite ordering during the martensitic transformation; it is inherited ordering. The parent phase of NiTi has a CsCl type B2 superlattice, while the product phase has a three-dimensionally close packed structure, monoclinic or B19', as depicted in Fig. 2.1 and Fig. 2.6. The main geometrical characteristics of the parent and product phases of NiTi alloy are stated in the Tab. 2.1.

Lattice parametres	Length (Å)			Angle (°)		
	a	b	c	ab	bc	ca
Martensite	4.678	4.067	2.933	90.00	90.00	98.26
Austenite	4.262	4.262	3.014	90.00	90.00	90.00

Table 2.1: Characteristic lattice parameters for NiTi alloys [8] for austenite a,b = $c/\sqrt{2}$ which is lattice correspondence cell of austenite, see Fig. 2.6; adapted from [5]

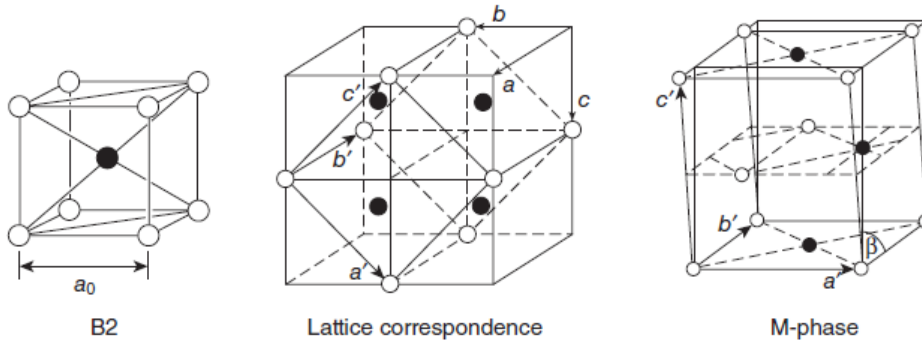


Figure 2.6: Crystal structures of the parent (B2) and martensite (B19') phases and the lattice correspondence between the two phases; taken from [4]

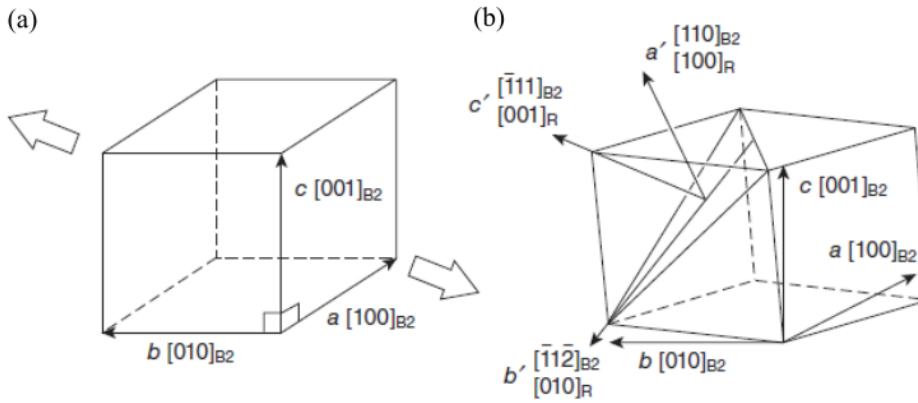


Figure 2.7: Crystal structure of the R-phase: (a) B2, (b) R-phase formed by elongation along one of $\langle 111 \rangle$ directions of B2 lattice; taken from [4]

In NiTi can occur, depending on heat treatment and alloy composition, a multistep martensite transformation with an intermediary phase formed upon cooling prior to the martensitic transformation. The intermediary phase is a rhombohedral phase, called the R phase. R phase is considered to be a martensitic transformation with low hysteresis and a small memory effect; for the R phase to appear, M_s must be lowered by some means. The microstructures that cause the R phase are explained in [12, 13].

The gradual decrease in temperature first transforms the austenitic B2 phase into the R phase and the martensitic B19' phase. The R phase can be formed by elongating along any one of the $\langle 111 \rangle$ direction of the B2 structure, as shown in Fig. 2.7. Since transformation hysteresis is much greater in the transformation B19' to B2 than in transformation R to B2, the reverse transformation omits the R phase. The R transformation is characterised by a small lattice distortion compared to the martensitic transformation. The small transformation strain (deformation) in the R-phase ($\sim 1\%$) compared to B19' ($\sim 8\%$) [14] leads to R-phase stabilisation at the expense of suppression of B19'.

The following factors support the existence of the R phase [15]:

- Substitution of a few percent of Ni by Fe or Al
- Reheating after low-temperature deformation
- Formation of precipitates Ti_3Ni_4 by ageing NiTi with a high Ni content

NiTi-based alloys are near-equiatomic and have the following properties:

- M_s temperature is dependent on the Ni content; see Fig. 2.8; The maximum possible temperature M_s is around 70 °C, below 50% Ni remains the M_s maximal independently of the composition, with an increase in the Ni content above at. 49.7% Ni the M_s decreases
- Strain induced by the martensitic transformation shows a strong orientation dependence [16, 17, 18]; generally the most favourable martensite variant grows to induce the maximal reversible transformation strain
- Stress-strain curves and consequently elastic moduli are temperature dependent [19]
- For monoclinic martensite, as is in the case of the B19' phase in NiTi, there exist 24 different crystal orientations, i.e. variants, with respect to B2 austenite. [20, 6]

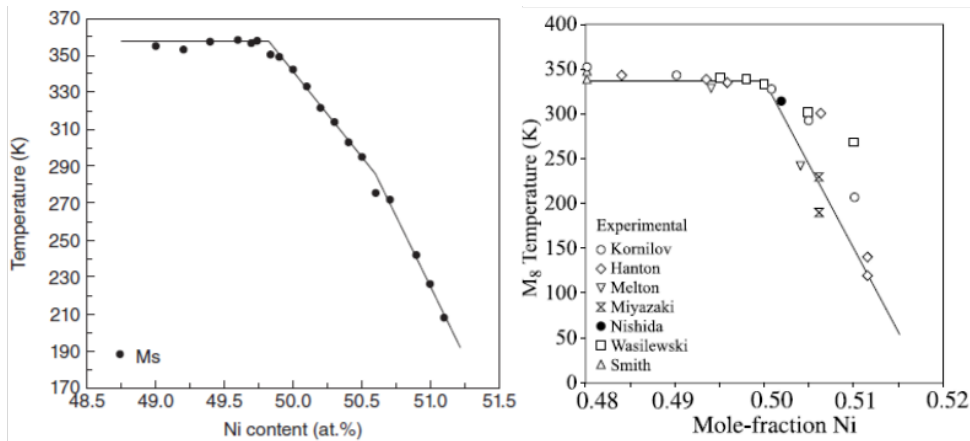


Figure 2.8: Ni content dependence of M_s temperature: (a) in atomic percent, taken from [5], (b) in mole fraction, taken from [15] which adapted [21]. The various symbols correspond to various experimental measurements, the line corresponds to a thermodynamic calculation

■ 2.3.1 NiTi thin films

SMA demonstrate prolonged periods of heat transfer in bulk. However, they are often used as actuators which are elongated by the means of martensitic phase transformation. Therefore, shorter period of heat transfer in order to

obtain fast response to temperature change is desirable. Such an improvement can be mediated by utilizing thin films since, compared to bulk, SMA thin films show significant changes in properties during phase transformation.

Large forces for actuation and large displacement makes the NiTi thin films favourable for applications in MEMS focused on microactuators [22], e.g. cantilevers, microvalves, microgrippers, springs, etc. Also, since NiTi thin films are sensitive to changes in environment such as temperature and stress, they can be utilized in microsensors [23, 24].

Sputtering was studied since the early 1990s as a possible deposition method to fabricate high quality thin films which would possess stable shape-memory characteristics and endure high stress to be used in practical applications [25]. Metallurgical factors and sputtering conditions strongly affect transformation and shape memory characteristics of sputtered NiTi thin films, for more details see [26, 27]. For an equiatomic NiTi thin film, the maximal elongation accounted for more than 40 % and for martensitic phase, the yield stress can be as high as 600 MPa and fracture stress can reach up to 800 MPa [28].

NiTi thin films prepared by epitaxy enable studying of NiTi monocrystals which are normally not available. While in polycrystals only an effective elasticity can be determined, study of such an epitaxial film may allow to find elastic constants of the martensite unit cell.

Chapter 3

Wave propagation in solids

If elastic waves propagate through an anisotropic solid, such as a crystal, with dimensions much larger than those of the beams of the waves propagating through, the crystal can be regarded as a continuous medium. The propagation of elastic waves through such a medium will be discussed in detail, based on [29] if not stated otherwise.

3.1 Hooke's law

Exposure of material to external forces, i.e., a mechanical contact at the surface or an applied field in the volume, can induce a relative displacement of the particles to each other; the gradient of displacement du_i/dx_j is nonzero. The emerged deformation can be described with a strain tensor S_{ij} of rank two. Since the strain excludes by definition an overall movement retaining the distances between the particles, i.e. translation or rotation, the small-strain tensor, i.e. strain tensor assuming small deformations, must be symmetric:

$$S_{ij} = \frac{1}{2} \left(\frac{\partial u_i}{\partial x_j} + \frac{\partial u_j}{\partial x_i} \right). \quad (3.1)$$

The displaced particles in the deformed solid are subjected to intermolecular mechanical traction forces, which tend to restore the original state of mechanical equilibrium. Mechanical traction $T(l)$ on a surface with arbitrary orientation l is described with a stress tensor T_{ij} of rank 2. In the absence of externally applied torque, the tensor is symmetric $T_{ij} = T_{ji}$, with only six independent components:

- normal to faces T_{ii} representing traction or compression,
- tangential T_{ij} representing shear forces.

When the external forces responsible for deformations are removed, an elastic solid returns to its initial state of zero strain and stress. Since small deformations are assumed, elastic behaviour is well described by a first-order term of a Taylor expansion for the relation between strain and stress. Since $T_{ij}(S_{ij} = 0) = 0$, the Taylor expansion becomes a one-to-one relation between strain S_{ij} and stress T_{ij} in an elastic solid, and Hooke's law takes form:

$$T_{ij} = c_{ijkl} S_{kl}. \quad (3.2)$$

The linear relation between the second-rank tensors T_{ij} and S_{kl} is expressed by a fourth-rank stiffness tensor c_{ijkl} . Due to the symmetry of T_{ij} and S_{kl} , the elastic constants hold $c_{ijkl} = c_{jikl}$ and $c_{ijkl} = c_{ijlk}$. Consequently, the Hooke law in terms of displacements takes the form:

$$T_{ij} = c_{ijkl} \frac{\partial u_l}{\partial x_k} \quad (3.3)$$

and the number of independent elastic constants is reduced from 81 to 36. Voigt notation reducing order of symmetric tensors by defining new indices $\alpha(ij), \beta(kl)$ as functions of the original indices i, j, k, l :

$$\begin{aligned} 1 &\leftrightarrow (11) & 2 &\leftrightarrow (2) & 3 &\leftrightarrow (33) \\ 4 &\leftrightarrow (23) = (32) & 5 &\leftrightarrow (13) = (31) & 6 &\leftrightarrow (12) = (21) \end{aligned} \quad (3.4)$$

can be applied. Both notations $c_{\alpha\beta} = c_{ijkl}$ can describe the 6x6 matrix of 36 independent elastic moduli. Energetic considerations lead to further symmetry of elastic constants about the main diagonal: $c_{\alpha\beta} = c_{\beta\alpha}$, consequently the matrix takes the form:

$$c_{\alpha\beta} = \begin{pmatrix} c_{11} & c_{12} & c_{13} & c_{14} & c_{15} & c_{16} \\ c_{12} & c_{22} & c_{23} & c_{24} & c_{25} & c_{26} \\ c_{13} & c_{23} & c_{33} & c_{34} & c_{35} & c_{36} \\ c_{14} & c_{24} & c_{34} & c_{44} & c_{45} & c_{46} \\ c_{15} & c_{25} & c_{35} & c_{45} & c_{55} & c_{56} \\ c_{16} & c_{26} & c_{36} & c_{46} & c_{56} & c_{66} \end{pmatrix} \quad (3.5)$$

As seen, the 36 independent components are further reduced to 21, which is a maximal number for a crystal whose centre of symmetry imposes no restriction, meaning triclinic. Crystal symmetry can further reduce the number of independent components.

3.1.1 Effect of crystal symmetry on the number of independent elastic constants

Each crystal structure belongs to one of 32 crystal classes according to its symmetry elements. Symmetry affects the stiffness tensor: the higher the symmetry, the less independent components.

The monoclinic system with a dyad axis, direct or inverse, leads to 13 independent constants:

$$c_{\alpha\beta} = \begin{pmatrix} c_{11} & c_{12} & c_{13} & 0 & 0 & c_{16} \\ c_{12} & c_{22} & c_{23} & 0 & 0 & c_{26} \\ c_{13} & c_{23} & c_{33} & 0 & 0 & c_{36} \\ 0 & 0 & 0 & c_{44} & c_{45} & 0 \\ 0 & 0 & 0 & c_{45} & c_{55} & 0 \\ c_{16} & c_{26} & c_{36} & 0 & 0 & c_{66} \end{pmatrix} \quad (3.6)$$

The tetragonal system leads to 6 independent constants:

$$c_{\alpha\beta} = \begin{pmatrix} c_{11} & c_{12} & c_{13} & 0 & 0 & 0 \\ c_{12} & c_{11} & c_{13} & 0 & 0 & 0 \\ c_{13} & c_{13} & c_{33} & 0 & 0 & 0 \\ 0 & 0 & 0 & c_{44} & 0 & 0 \\ 0 & 0 & 0 & 0 & c_{44} & 0 \\ 0 & 0 & 0 & 0 & 0 & c_{66} \end{pmatrix} \quad (3.7)$$

The cubic system with at least four triad axes and three direct dyad axes leads to 3 independent constants:

$$c_{\alpha\beta} = \begin{pmatrix} c_{11} & c_{12} & c_{12} & 0 & 0 & 0 \\ c_{12} & c_{11} & c_{12} & 0 & 0 & 0 \\ c_{12} & c_{12} & c_{11} & 0 & 0 & 0 \\ 0 & 0 & 0 & c_{44} & 0 & 0 \\ 0 & 0 & 0 & 0 & c_{44} & 0 \\ 0 & 0 & 0 & 0 & 0 & c_{44} \end{pmatrix} \quad (3.8)$$

3.2 Christoffel's equation

A combination of an equation of propagation through a solid, where the displacement u_i of an arbitrary point with coordinates x_k varies with time as $u_i = u_i(x_k, t)$, with the Hooke law leads to a wave equation:

$$\rho \frac{\partial^2 u_i}{\partial t^2} = c_{ijkl} \frac{\partial^2 u_l}{\partial x_j \partial x_k}. \quad (3.9)$$

One possible solution of the wave equation has the form of a plane wave:

$$u_i = {}^\circ u_i F\left(t - \frac{n_j x_j}{V}\right), \quad (3.10)$$

where ρ is a solid density, ${}^\circ u_i$ is wave polarisation, V is a phase velocity, and n is a unit vector of direction of propagation. Substitution of the solution into the wave equation leads to Christoffel's equation:

$$\rho V^2 {}^\circ u_i = \Gamma_{il} {}^\circ u_l, \quad (3.11)$$

where $\Gamma_{il} = c_{ijkl} n_j n_k$ is symmetric Christoffel's tensor of rank two, ${}^\circ u_i$ is an orthogonal eigenvector of Γ_{il} and $\gamma = \rho V^2$ is a positive eigenvalue. To conclude, solving the Christoffel equation provides characteristics of the plane wave propagating in direction n in a crystal with stiffness c_{ijkl} :

- a phase velocity in the form of the eigenvalue of the Christoffel's tensor Γ_{il}
- a polarization, i.e. the direction of displacement, in the form of the corresponding eigenvector of Γ_{il} .

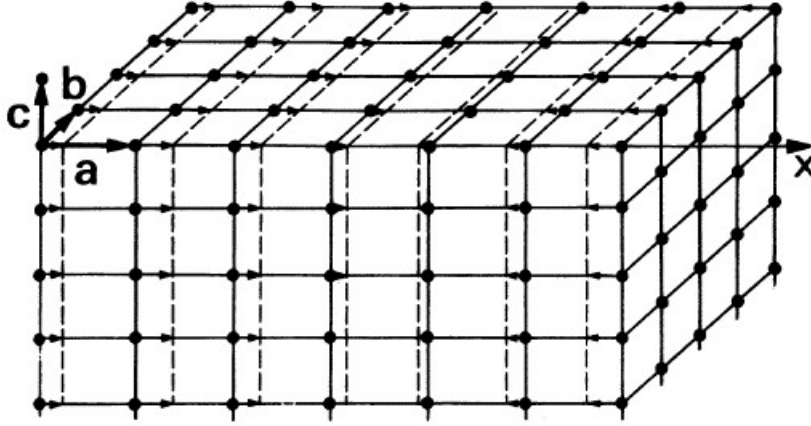


Figure 3.1: Deformation of a crystalline lattice during propagation of a longitudinal wave parallel to the row vector \mathbf{a} ; taken from [29] It is sufficient to consider the displacements of the atoms in one row.

Since Christoffel's equation consists in fact of three homogeneous equations, the solution provides three phase velocities for a given direction. Therefore, in one direction three plane waves can propagate with different velocities and mutually orthogonal polarizations, as discussed in subsection 3.2.1 below.

Note that the symmetry of the crystals in which propagation takes place in a specific direction affects the number of components of the Christoffel's tensor as it affects the number of independent components of the stiffness tensor.

■ 3.2.1 Wave polarisation

Wave polarisation, i.e. the atomic displacement direction with respect to propagation direction, can be both longitudinal, i.e. parallel to the propagation direction \mathbf{n} , and transverse, i.e. perpendicular to the propagation direction \mathbf{n} , see Fig. 3.1 (longitudinal polarisation along basis vector \mathbf{a} of the atomic lattice, transverse polarisation along one of the basis vectors \mathbf{b} or \mathbf{c}). With each polarisation are connected different restoring forces; therefore, for a propagation along \mathbf{a} , as in Fig. 3.1, there are three distinct wave types:

- longitudinal wave L , polarised along \mathbf{a} ,
- transverse (shear) wave T_1 , polarised along \mathbf{b} ,
- transverse (shear) wave T_2 , polarised along \mathbf{c} .

In a special case of crystallographically equivalent directions \mathbf{b} and \mathbf{c} , the two transverse waves propagate along with the same velocity. Propagation of the three waves along \mathbf{b} or \mathbf{c} is also possible, however, with different velocities due to a phase velocity dependence on the wave vector direction. Purely longitudinal or transverse waves are quite rare, as, generally, the displacement vector \mathbf{u} points in a direction other than parallel or perpendicular to the

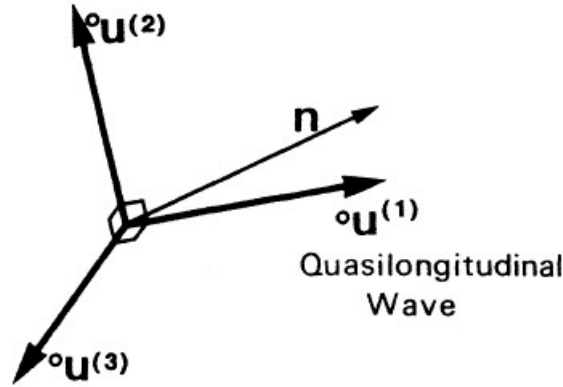


Figure 3.2: Propagation in an anisotropic crystal; taken from [29]. In general, three plane waves can propagate in the same direction \mathbf{n} , each with its characteristic velocity. The one whose polarisation (material displacement) ${}^{\circ}\mathbf{u}^{(1)}$ is closest to the wave vector \mathbf{n} is called a quasi-longitudinal wave. Its velocity is usually higher than that of the other waves, called quasi-transverse, which have polarizations ${}^{\circ}\mathbf{u}^{(2)}$ and ${}^{\circ}\mathbf{u}^{(3)}$. The three vectors ${}^{\circ}\mathbf{u}^{(1)}$, ${}^{\circ}\mathbf{u}^{(2)}$, ${}^{\circ}\mathbf{u}^{(3)}$ are mutually perpendicular.

propagation direction \mathbf{n} , i.e. the wave vector \mathbf{k} ; see Fig. 3.2. If the wave vector is inclined for example again to the vector \mathbf{a} , according to the wave polarisation position in relation to the propagation vector, still three waves propagate:

- one quasi-longitudinal wave qL, with polarisation closest to the propagation vector \mathbf{n} ,
- two quasi-transverse waves qT, with polarisation perpendicular to qL and mutually differing velocities.

■ 3.2.2 Characteristic surfaces

In a crystal, the (quasi) longitudinal wave propagates with velocity $V_L = V_1$ and the (quasi) transverse waves propagate with velocities $V_T = V_2, V_3$, where $V_2 \neq V_3$. In an isotropic solid, because the tensor Γ is independent of the propagation direction, there are only two velocities:

$$V_L = \sqrt{\frac{c_{11}}{\rho}}, \quad V_T = \sqrt{\frac{c_{44}}{\rho}} = \sqrt{\frac{(c_{11} - c_{44})}{2\rho}}. \quad (3.12)$$

The (q)L waves propagate faster than the (q)T waves in a crystal; in an isotropic solid holds:

$$V_T < \frac{V_L}{\sqrt{2}}. \quad (3.13)$$

The propagation of elastic waves in crystals can be visualised with several characteristic surfaces as a function of direction; three surfaces for an anisotropic solid and two spheres for an isotropic solid.

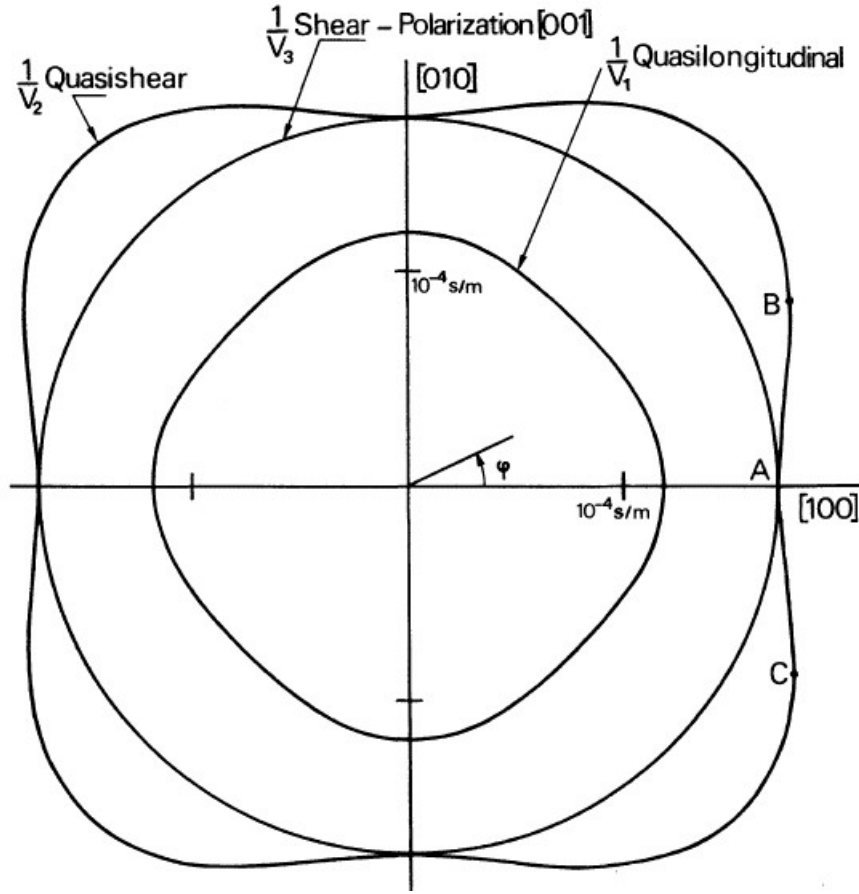


Figure 3.3: Slowness surface of cubic system illustrated for silicon (m_{3m} , anisotropy factor 1.565) in the (001) plane; taken from [29]

When from an origin O there are vectors drawn for different directions $\mathbf{V} = V\mathbf{n}$ with length equal to the phase velocity V of waves having wavefronts perpendicular to the propagation directions \mathbf{n} , the ends of the three vectors corresponding to one quasi-longitudinal wave (V_1) and two quasi-transverse waves (V_2, V_3) compose the velocity surface.

The velocity surface is related by the inversion through the origin to the slowness surface. In addition to the inverse phase velocities ($1/V_1, 1/V_2, 1/V_3$), the slowness surface provides information about the direction of energy flow as the energy velocity is normal to the slowness surface at all points. Consequently, if the plane of the slowness surface drawing is also a symmetry plane for the elastic properties, it contains the surface normal and hence the energy vector. The propagation direction is specified by the two polar angles θ and φ . An example of slowness surface, obtained by solving the Christoffel's equation for a cubic system of silicone when the propagation is along the cube face, is depicted in Fig. 3.3-

When from an origin O are for different directions drawn energy velocity vectors V^e showing the directions of energy transport, i.e. the directions of

acoustic rays, the locus of points traced by the end of these vectors defines a wave surface.

The energy velocity V_i^e for a displacement with unit magnitude, $u_i = 1$ shows the direction of energy transport and can be calculated using the following formula:

$$V_i^e = \frac{c_{ijkl} \circ u_j \circ u_l n_k}{\rho V}. \quad (3.14)$$

Since $\mathbf{V}^e \mathbf{n} = V$, a projection of the energy velocity onto the propagation direction is equal to the phase velocity, consequently the phase velocity is at most equal to the energy velocity.

To conclude, free propagation of elastic waves in a crystal is preferably characterised by the simplest of the surfaces, the slowness surface, see [31] for more details. The slowness surface is composed of three surfaces. For each of the three types of waves (L, T_1, T_2), each slowness surface shows the inverse phase velocity for a given direction as well as the direction of energy flow.

3.3 Guided waves

Bulk waves are assumed to propagate without encountering any boundaries in the crystal. The presence of a surface or interface in the crystal leads to a reflection accompanied by a change of direction and often wave type. A wave propagating by reflection between two parallel surfaces of a plate or along a free simple surface is called a guided wave.

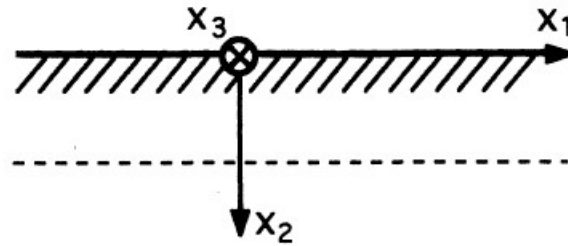


Figure 3.4: A semi-infinite crystal with a surface plane (x_1, x_3) located in the region $x_2 > 0$. If the broken line defines a surface plane as well, the crystal is bounded by two parallel planes; taken from [29].

Assume a crystal as pictured in Fig. 3.4 . The (x_1, x_2) plane, containing the surface normal and the propagation direction x_1 , is called a sagittal plane. If the crystal has properties constant in time and along the propagation direction x_1 , linear behaviour and no attenuation, the normal modes have the following form:

$$u_i(x_i, t) = u_0(x_2, X_3) e^{i(\omega t - kx_1)}, \quad (3.15)$$

where u_i is one of the components of the mechanical displacement u . From equations of propagation, where the unknown are three components of mechan-

ical displacement, and from boundary conditions imposed by the structure are derived various propagation modes at the given conditions. Crystal symmetry can make the equations split into two independent parts; two special families of modes emerge:

- modes with displacement components contained in the sagittal plane,
- modes with a single transverse component parallel to the surface.

Without crystal symmetry, the two types of modes combine. Let us consider a simple case in which the sagittal plane (x_1, x_2) is normal to a dyad axis, which is thus along x_3 . Two specific cases are considered, a direct A_2 or inverse axis normal to the sagittal plane, the latter being equivalent to a mirror plane M parallel to the sagittal plane. The conclusions, types of waves propagating in the directions and their characteristics, are summarised in the Tab. 3.1:

Sagittal plane orientation	$\perp A_2$	$\parallel M$
Type of wave	P_2	TH
Wave polarization	in the plane (x_1, x_2)	u_3
Displacement component	$u_3 = 0$	$u_1 = u_2 = 0$
Mechanical stress component	$T_{22}, T_{12} \neq 0, T_{32} = 0$	$T_{22}, T_{12} = 0, T_{32} \neq 0$

Table 3.1: Type of elastic waves propagating in two special cases, sagittal plane perpendicular to A_2 or parallel to M , adapted from [29]. A_2 is a direct axis of even order, M is a mirror plane, TH denotes transverse horizontal wave with polarisation u_3 and P_2 wave polarised in the sagittal plane. The plane (x_1, x_2) is sagittal plane.

The above results relate to a variety of structures. For the two symmetric cases, specific wave types propagating in various waveguides are discussed in following sections in detail.

■ 3.3.1 Free surface

The simplest propagation medium is an isotropic semi-infinite solid with a free surface.

Rayleigh wave R_2 is polarized in the sagittal plane and has two displacement components. The mechanical stresses T_{12} and T_{22} , zero on the free surface, couple the two components u_1 and u_2 . Therefore, the decrease in u_2 with depth implies a decrease in u_1 , and the Rayleigh wave remains close to the surface as it propagates and is guided along the surface. However, since the two displacement components have a phase difference of $\pi/2$, the polarisation is elliptical, and so their amplitudes decrease with depth at different rates. The undulation of the surface, caused by wave propagation, extends to a depth of the order of wavelength λ , as illustrated in Fig. 3.5. Considering that the solid behaves less rigidly in the absence of material above the surface, the Rayleigh wave velocity V_R is slightly less than the velocity V_T of the bulk transverse waves.

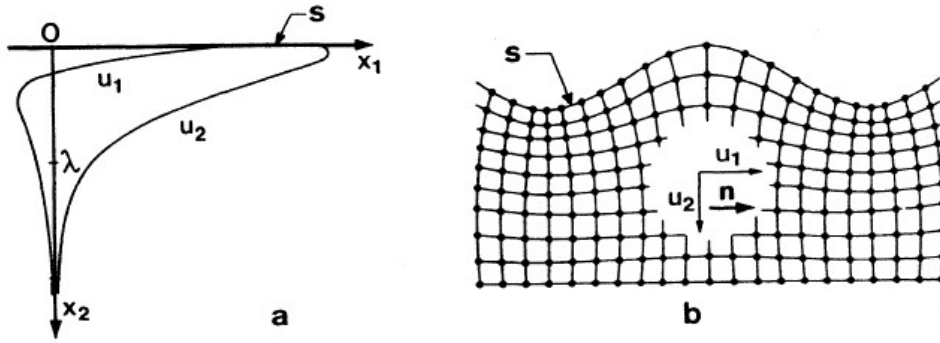


Figure 3.5: Rayleigh wave R_2 in an isotropic semiinfinite solid, where s is the free surface and \mathbf{n} is the propagation direction: a) Decrease of the longitudinal and transverse components u_1 and u_2 with depth, b) Displacement of the surface; taken from [29]

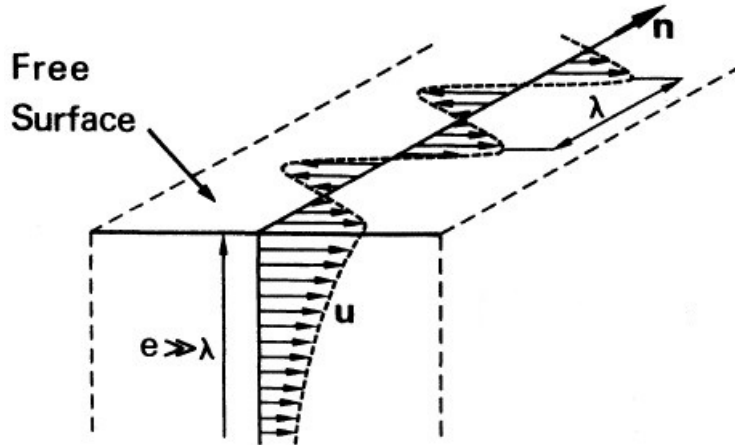


Figure 3.6: TH- type surface wave with transverse horizontal polarization. The surface of the solid remains flat; taken from [29]

Transverse horizontal wave TH has an amplitude that decreases with depth. The penetration depth, some tens of wavelengths, is always greater than that of Rayleigh waves; see Fig. 3.6.

If the symmetry elements (A_2 or M) of the crystal are orientated differently, numerical calculations are needed. A generalized Rayleigh wave R_3 , coupling R_2 and TH waves and thus having three components of displacement instead of two, propagates near the surface. The velocity depends on the crystal cut and the direction of propagation.

Pseudo-surface wave, or pseudo-Rayleigh wave, arises when crystal's anisotropy causes the Rayleigh wave to move faster than the bulk vertically or horizontally polarised transverse waves (TV, TH, respectively).

In case of a crystal with a cubic symmetry, the TV wave velocity is independent of direction, while the quasi-TH wave velocity $V_{TH}(\theta)$ is direction dependent - θ is the angle between propagation direction and plane [100]- and

it holds $V_{TH}(0) = V_{TV}$. Since the TH wave propagates in a direction given by the planes of symmetry (010) and (1 $\bar{1}$ 0), it is not coupled to the Rayleigh wave's displacement confined to the sagittal plane while propagating along [100] or [110]. The velocity of such a Rayleigh wave may be higher than that of the TH wave. The size of anisotropy factor A affects the relative velocities of the propagating waves:

- $A < 1$ and $V_{TH}[110] > V_{TV}$, see Fig. 3.7a The TH-wave velocity $V_{TH}(\theta)$ increases with θ with a maximum value in the [110] direction. Due to a weak coupling between the TH wave and the Rayleigh wave, $V_R(\theta) < V_{TV}$
- $A > 1$ and $V_{TV} > V_{TH}[110]$, see Fig. 3.7b. With increasing θ , the TH wave velocity $V_{TH}(\theta)$ drops with θ to a minimal value along the [110] direction, where $V_{TH} < V_R(\pi/4)$, while the coupling between the two waves increases. When the TH and Rayleigh waves encounter, the Rayleigh wave degenerates into two waves, the original Rayleigh wave with $V_{TH} < V_R$ and a new surface wave, called pseudosurface wave, with $V_R > V_{TH}$ and no confinement near the surface due to supporting the increase in the TH wave.

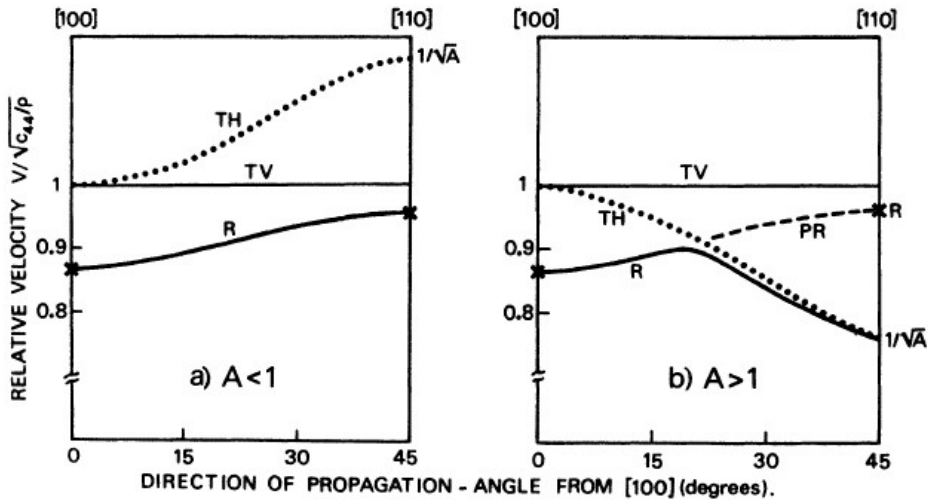


Figure 3.7: Propagation of surface waves, of type Rayleigh (R) or pseudo-Rayleigh (PR), along the (001) plane of a cubic crystal. The anisotropy factor A is: a) less than, or b) greater than unity. Where the Rayleigh wave is denoted by a cross, it is not coupled to the bulk TH wave, so its velocity can be greater than V_{TH} ; taken from [29]

3.3.2 Plate

Lamb wave L_2 is an analogue of a Rayleigh wave, however unlike the Rayleigh normal guided wave with two components propagating through a free surface, the Lamb wave propagates through a free plate, i.e. an isotropic solid bounded by two parallel free surfaces. While the Rayleigh wave R_2 propagates independently on each free surface if the thickness is much larger

than the wavelength λ , when the thickness of the plate h becomes comparable to λ , the longitudinal and transverse components of the R_2 waves are coupled, leading to symmetric or antisymmetric deformations of the plate, as in Fig. 3.8.

The isotropic plate is also a waveguide for the transverse TH wave, Fig. 3.9.

A free-surfaced crystalline plate, with one of the symmetries considered above, can guide waves of type L_2 and TH, plus, if $h \gg \lambda$, the R_2 waves.

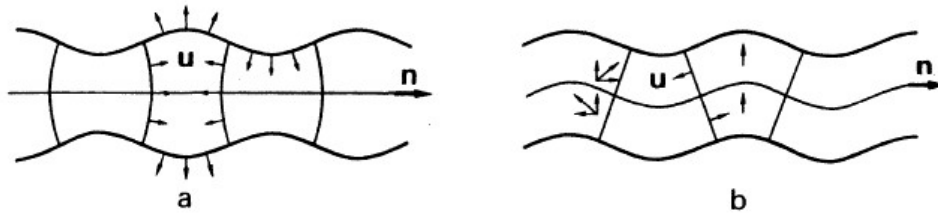


Figure 3.8: Lamb waves in an isotropic plate, showing deformations of the plate ofor: a) symmetric mode and b) antisymmetric mode; taken from [29]

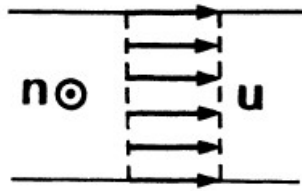


Figure 3.9: Another mode of the plate, the purely transverse TH wave. The mode of order zero is shown; taken from [29]

3.3.3 Film-substrate system

A film on a substrate, with a free surface on one side and a solid-solid interface on the other, can be considered an intermediate case between the free surface and a plate between two planparallel surfaces. In this case, the energy of the wave propagates partially in the film and partially in the substrate.

Since the penetration depth of surface wave typically depends on its wavelength (and thus, frequency), the influence of the substrate changes. It can be neglected if wavelengths much shorter than the film thickness are used, which allows a direct study of the film properties. On the other side, the influence of the film can be neglected if the wavelengths are much longer than the film thickness.

Nevertheless, even the intermediate frequencies (i.e., wavelengths comparable to the film thickness) can be used to characterize the film properties in the case of known substrate elastic properties.

The character of the frequency dispersion depends on the velocity of wave propagation in the film relative to the substrate.

■ Fast film on slow substrate

If the Rayleigh-type SAWs propagate faster in the film than in the substrate, the Rayleigh-type SAWs velocity increases with an increasing frequency until the the frequency is sufficient for the Rayleigh-type SAWs velocity to match the bulk qT wave velocity in the substrate, at which point the Rayleigh-type SAW gradually transforms into the qT wave in the substrate and does not propagate on higher frequencies – until such high frequencies where the substrate influence is suppressed. Therefore, only limited information is available on Rayleigh-type SAW frequency dispersion in a given frequency region.

■ Slow film on fast substrate

If the Rayleigh-type SAWs propagate slower in the film than in the substrate, the low frequency Rayleigh-type SAWs begin propagating with a velocity of the substrate, since the penetration depth (scaling with wavelength) is large and thus the film has only little influence. Increase in frequency, corresponding to shorter wavelengths, weakens the substrate influence and the velocity of Rayleigh-type SAWs drops gradually to the level of the Rayleigh-type SAWs velocity in the film, see Fig. 3.10.

Sezawa waves are another wave modes which occur at certain cut-off frequencies and propagate with velocity higher than the Rayleigh wave but lower than that of the bulk waves in the substrate. The character of Sezawa waves is similar to that of the Rayleigh wave, but Sezawa waves have more pronounced longitudinal displacement and are thus faster. They oscillate in the film itself and attenuate quickly into the depth of the substrate.

The Love wave, shown in Fig. 3.11, is a dispersive transverse horizontal wave which propagates in a system where the bulk transverse wave in the film is slower than the bulk transverse wave in the substrate.

Although an analytical model for calculation of wave velocities in isotropic film-on-a-substrate systems was presented [32], it leads to sets of equations which are typically solved numerically. For anisotropic systems, the problem is more complex as the wave modes couple together in non-principle directions, and thus other calculation approaches are necessary. An approach based on the Green's function can be used [30]. Another possibility is a numerical Ritz-Rayleigh method described in chapter 5.

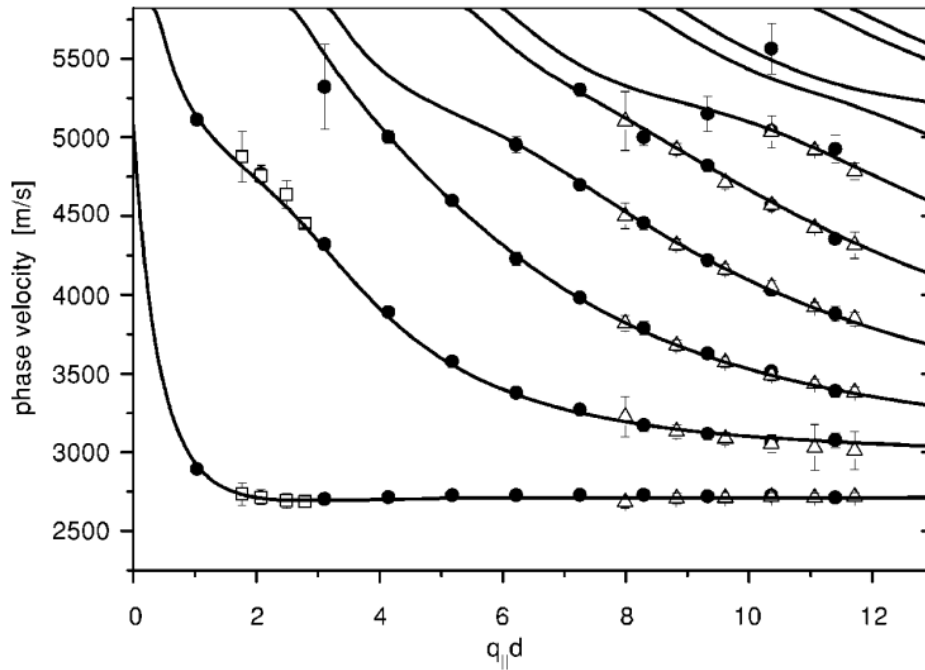


Figure 3.10: Phase velocity dispersion curves of Rayleigh (the lowest branch; RW) and various orders of Sezawa (the higher branches; SW) waves in a slow-on-fast system of WC film on silicon substrate, where q_i is the surface wave vector (otherwise marked as $k_{||}$) and d is the film thickness. Measured data for various film thicknesses and scattering angles is shown by the symbols, the lines represent the computed best fit to the experimental data, taken from [33]. While the displacement field of RW extends mainly near the free surface, it extends throughout the film in case of SW and descends exponentially in the substrate. Due to the RW localization close to the film surface to which the surface dynamical response pertains, RW has a higher intensity than SW. The higher the $q_i d$, the more SW is supported by the film.

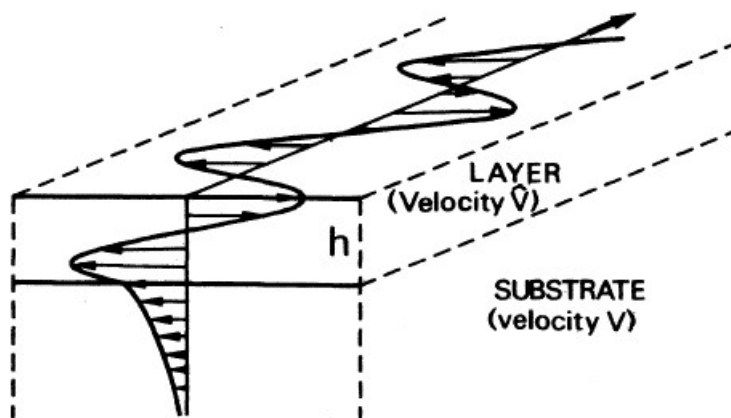


Figure 3.11: The Love wave, a transverse wave propagating in a layer and its supporting substrate, provided $V_T > V_T^f$. The penetration depth into the substrate is high at low frequencies, when $\lambda \gg h$; taken from [29]

Chapter 4

Laser-ultrasonics

In this chapter are described generation of the various types of elastic waves introduced in chapter 3 and detection of the surface mechanical displacements caused by these elastic waves.

4.1 Photothermal generation

The Nd:YAG laser is one of the most common optical sources exploited for generating elastic waves in metals. Laser light pulses focused in a line on the surface of a semi-infinite solid act as a line source that generates simultaneously various bulk and surface plane waves, see chapter 3.

The mechanical perturbations induced in the elastically isotropic material by irradiation are depicted in Fig. 4.1. Perturbations localised on semi-circle of radii $V_T t$ and $V_L t$ correspond to transverse (shear) and longitudinal waves, respectively. Perturbations located on the free surface $x_3 = 0$ at the distance $x_1 = \pm V_R t$ correspond to the Rayleigh waves. Perturbation in the region $|\theta| < \theta_c$, where θ_c is the critical angle defined relative to the free surface normal as:

$$\sin \theta_c = \frac{V_T}{V_L}, \quad (4.1)$$

corresponds to a lateral wave, i.e., head wave, with wave fronts parallel to the line LT in Fig. 4.1. The head wave propagates on the free surface with the same speed as the longitudinal wave, therefore it is also called the surface-skimming longitudinal wave, and its amplitude decreases with distance from the source more rapidly than the Rayleigh wave (as its energy radiates into the below of the surface, i.e. into the bulk).

There are two mechanisms of elastic wave generation, depending on the power density of a light pulse that impacts a free surface of an opaque solid.

- The thermoelastic regime takes place when the power density I (W/m^2) of the laser pulse causes no melting; the local expansion occurs through heating. The thermal expansion induces forces close to parallel to the free surface, see Fig.4.2a.

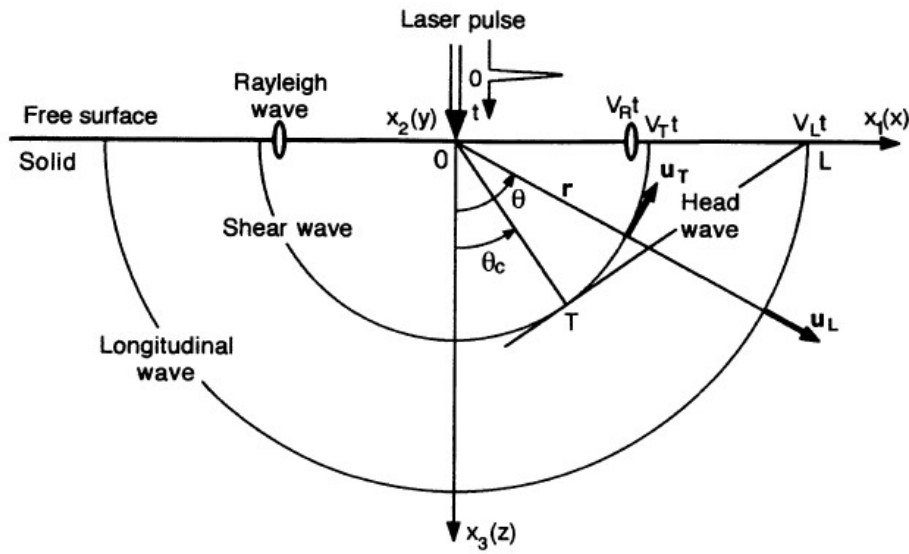


Figure 4.1: Wave fronts generated by a point or line source in a semi-infinite isotropic solid; taken from [34]

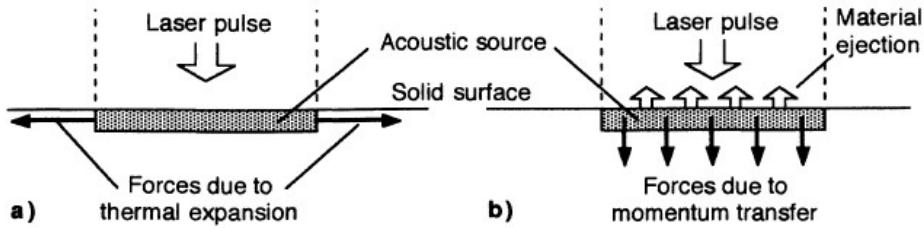


Figure 4.2: Photothermal generation: a) Thermoelastic regime, b) Ablation regime; taken from [34]

- The ablation regime takes place when absorption of a sufficient power density leads to melting followed by vaporisation of a small amount of material; the surface state is modified. Momentum transfer due to particle ejections induces forces normal to the surface in the irradiated zone, see Fig. 4.2b. The ablation regimes mostly generate longitudinal elastic waves.

In reality, both regimes of photothermal generation are present; for more information see [34]. In TGS, the thermoelastic regime is desired.

4.2 Transient Grating Spectroscopy

Transient grating spectroscopy (TGS; also known as impulse stimulated thermal scattering (ISTS) [35]), as seen in 4.3, is an experimental laser-ultrasonic technique exploited for contactless in situ detection of phase transformations in an examined material.

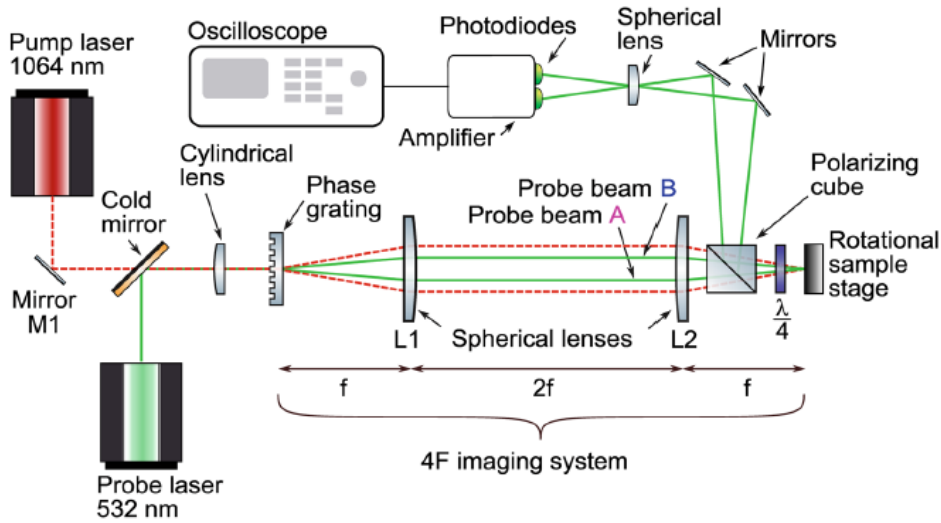


Figure 4.3: A diagram of the TGS setup; taken from [36]

The used TGS set-up involves optical excitation of narrowband SAWs by a Nd:YAG pump laser (1064 nm, pulse energy 200 μJ , nominal pulse duration 0.55 ns, pulse repetition rate 1000 Hz) and their detection by a probe laser (532 nm, nominal pulse power 100 mW). Both laser beams pass through a cylindrical lens and a diffraction grating.

The grating is optimized to have a maximal diffraction efficiency at the first diffraction orders for wavelengths of both laser beams, diffraction beams of all orders except for the first-order beams are blocked. First-order beams are projected by a 4F image system onto a sample surface with a 1:1 optical magnification.

Crossover of the coherent diffracted first-order beams on the free surface of the sample leads to interference. The spatial periodicity of the interference pattern is determined by the angle of incidence which can be adjusted by the transmission phase grating. Thus, simply changing the grating easily modifies the periodicity of the interference pattern. The resulting periodic array consists of pump laser beam lines spaced half a grating constant away; each of the lines acts as a line-like thermoelastic source to excite SAWs. Consequently, ultrasonic waves of constrained wave vectors are excited. Moreover, since the cylindrical lens focusses the laser beams into an elliptical shape instead of the original round shape, the excitation pattern has a prolonged, highly elliptical shape, and thus imposes even stronger constraint on the excited k -vector of the elastic waves.

The pulse laser energy spread over the array of photoacoustic sources prevents local ablation of the sample surface. The possibility to induce only reversible changes in the exposed surface together with the contactless nature of the measurement makes TGS well suited for repeated measurements at a single spot of a sample. Moreover, the pulse laser impact causes a local increase in temperature small enough to provide a reliable and accurate sample temperature control at the measured point.

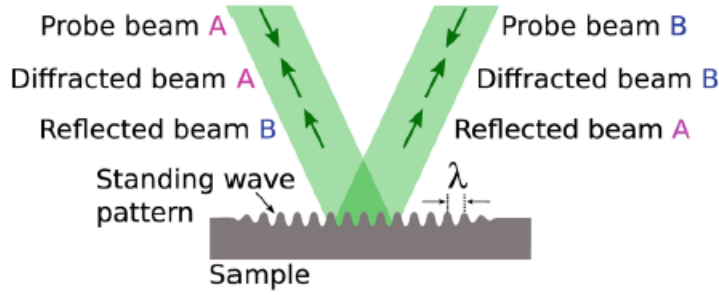


Figure 4.4: A diagram of probe beams in the Littrow configuration; taken from [36]

The excited SAWs propagate in opposite directions and superpose on the imposed surface into an array of standing waves with a dominant wavelength equal to the source line spacing, half a grating constant, and a dominant wave vector orientated perpendicular to the source lines. The array of standing SAWs acts as a time-dependent grating for a simultaneous detection described in the next paragraph. The time-dependent grating is also called transient grating, giving name to the method.

The two continuous-wave (CW) probe laser beams, separated by the diffraction grating and merged again on the sample surface, act as detection beams. Depending on the relative phase difference between the excitation and detection patterns, called the heterodyne phase, two grating modes apply. Amplitude grating mode, occurring when the excitation and detection patterns are precisely aligned on top of each other (i.e. in phase), refers to change in reflectivity. Since the change in reflectivity is negligible in case of irradiated metals, other grating mode is required. Phase grating mode enabling detection of the surface displacements is reached with a disalignment of the excitation and detection of their maxima and minima. The most favourable for SAW measurements is heterodyne phase equal to $\pi / 2$ [37, 38]. Instead of fine-tuning the heterodyne phase itself, it is possible to adjust the mirror M1 before each scanning measurement so that the excitation and detection patterns are in such a relative position as to obtain a maximal frequency-domain acoustic signal on the oscilloscope. Since the interference patterns produced are exactly the same, the excitation and detection wave-vector selectivity add up, and the sensitivity of the method to the given wave-vector increases.

The CW probe laser beam covers multiple wavefronts of the array. The probe laser beam diffracts on the wavefronts of the array and at the same time reflects from the sample surface. As the Littrow configuration is applied in the TGS setup and both first-order probe beams are symmetrical, each of them diffracts in the direction of reflection of the other one, as depicted in Fig.4.4. The standing-wave frequency is encoded in the form of intensity modulations of the diffracted probe beam, whereas the reflected probe beam serves as a reference in the following differential heterodyne detection.

A set of quarter-wave plate and a polarising cube split the pump and

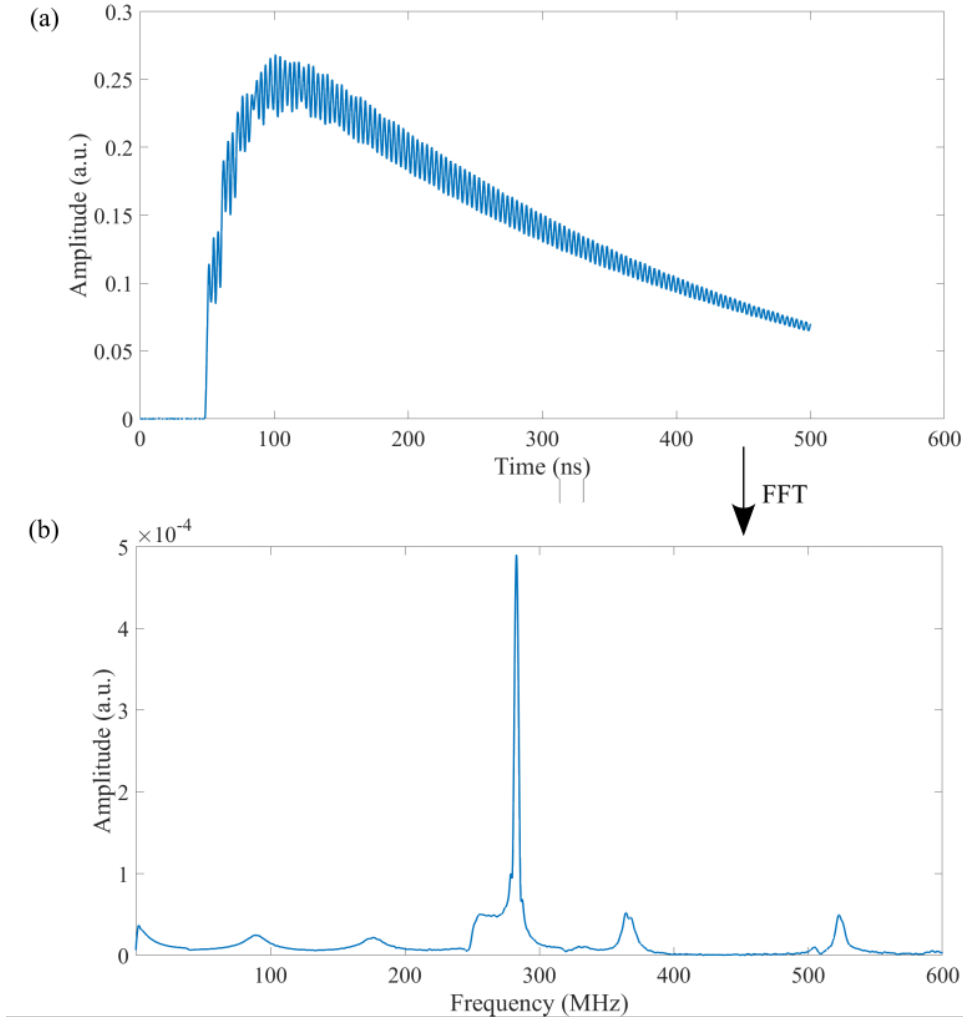


Figure 4.5: TGS signal of NiTi3100 at temperature of 111 °C, angle 20°, SAW wavelength 10 μm : (a) measured time-domain signal, (b) frequency spectrum calculated by FFT from time-domain signal (a)

probe beams. Only the probe beams pass through two high-speed Si pin photodiodes that record the probe beam intensity modulations. Due to the photodiode differential arrangement [39], the output voltages are subtracted, removing the phase-independent part of the signal, and amplified with a gain of 40 dB in the bandwidth range from 10 kHz to 2 GHz. Thus, the signal-to-noise ratio is improved, allowing the detection of even very slight out-of-plane oscillations of the examined surface. The signal, proportional to the instantaneous out-of-plane displacement, is recorded with a Teledyne LeCroy WaveRunner 640 Zi oscilloscope with a 4 GHz bandwidth and a vertical resolution of 8 bits.

To determine the SAW velocities, time profiles of the transient grating have to be obtained for each measured direction, see Fig. 4.5a. If, for each measured direction, several thousands of time-domain waveforms are averaged,

effective resolution is increased, and noise is reduced. Next, the averaged signal is subjected to a Fourier transform and the dominant frequency, Fig. 4.5b, obtained is used to calculate the SAW velocity for a given wave vector at any measured point according to the relation: $v = \lambda f$, where λ is the wavelength determined by the distance between source lines and f recorded frequency.

Entering the frequency spectra obtained from TGS (as shown in Fig. 4.5) for each measured angle (temperature) into one plot provides a so-called frequency map. Due to the simple recalculation of the frequency axis to velocity, a visualization of the frequency-domain signals and their evolution with angle (temperature) can be obtained in the form of velocity map as well. For visualization of the signal strength, the magnitude of the measured FFT amplitude/ calculated velocity for each measured angle (temperature), normalized to the overall highest value, is captured by colour code as shown in chapter 6.

Chapter 5

Ritz-Rayleigh numerical method

As discussed in the chapter 3, calculation of wave velocity in anisotropic materials is a rather difficult task. Even more so for the guided waves, which add boundary conditions to the problem, making it too complex to solve analytically except for special cases. Thus, numerical calculations were used to characterize the properties of Rayleigh waves in anisotropic materials [40].

A useful numerical approach was devised by Every et al. [41], calculating the surface response to a source of disturbance using Green's functions. Another suitable numerical method, presented in this work, is the Ritz-Rayleigh method, discussed by Stoklasová et al. [42].

The Ritz-Rayleigh method employs a discretization in the functional space, which transforms the wave problem into a linear eigenvalue problem. Thus, it can be used to determine SAW velocity for any direction of propagation in anisotropic media of arbitrary class of symmetry and arbitrary orientation of the free surface. Calculation of the velocities with the material properties known is called the forward method.

In order to characterize elasticity of the sample, the inverse method is needed, i.e., a method characterizing elasticity of the sample based on known wave velocities.

Note that the coordinate system is renamed here as: $x_1^{RR} = x_1^W$, $x_2^{RR} = x_3^W$, $x_3^{RR} = x_2^W$, where the superscript RR refers to chapter 5 and superscript W to section 3.3.

5.1 Forward problem

Analogously to the transient grating described in chapter 4.2, propagation of two plane waves propagating in opposite directions with identical wavelength λ and frequency ω results in superposition into a standing wave – a resonance of the free surface.

The resonant frequencies ω and corresponding modal shapes of displacement $\mathbf{u}(\mathbf{x})$ of a resonating body can be determined by the functional characterization by applying Hamilton's principle. The variational condition has the following form:

$$\frac{\partial}{\partial \mathbf{u}} \Lambda(\mathbf{u}, \omega) = 0, \quad (5.1)$$

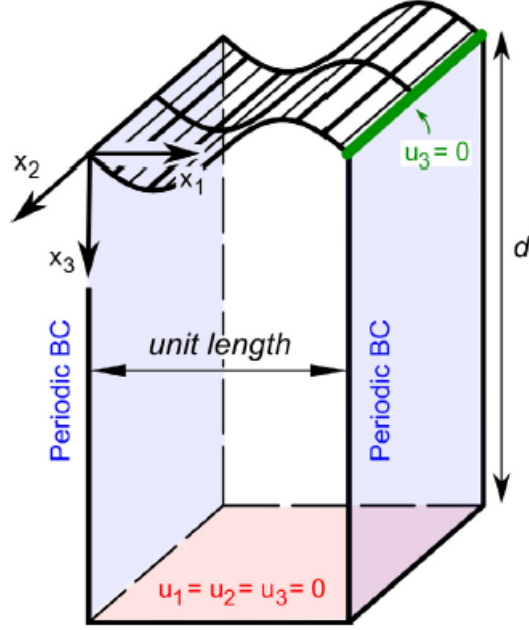


Figure 5.1: Computational domain with boundary conditions; taken from [42]

where Λ stands for the Lagrange energy of the resonating body vibrating harmonically at the frequency ω and is defined as:

$$\Lambda = \frac{1}{2} \int_0^1 \int_0^d \left(\rho \omega^2 u_i(\mathbf{x}) u_i(\mathbf{x}) - c_{ijkl} \frac{\partial u_i}{\partial x_j}(\mathbf{x}) \frac{\partial u_k}{\partial x_l}(\mathbf{x}) \right) dx_1 dx_3, \quad (5.2)$$

where c_{ijkl} is the material elasticity tensor in the chosen propagation direction, i.e., acquired by linear transformation of elastic constants related to the natural material coordinates into the orthogonal system of the considered resonating body.

The resonating body is modeled by a computational domain, adapted for the solved situation. The domain used for the surface-wave calculation is shown in Fig 5.1. The domain is defined by three directions x_1 , x_2 , x_3 . The domain size in the propagation direction x_1 is unitary, which enforces a harmonic solution with a unit wavelength in this direction. The harmonic solution gives a periodic condition:

$$\mathbf{u}(0, x_2, x_3) = \mathbf{u}(1, x_2, x_3). \quad (5.3)$$

The domain base is fixed by the condition in the form:

$$\mathbf{u}(x_1, x_2, d) = 0. \quad (5.4)$$

Thus, the domain depth, that is, the direction of the free surface x_3 or normal of the measured surface is taken such that fixed base does not affect the surface-wave propagation. Although the typical penetration depth of

SAWs in isotropic media is double the wavelength in direction x_1 , see section 3.3.1, this penetration depth can grow much larger for anisotropic media, and for pseudo-SAW propagation in particular. Hence, the factor of $d = 15$ is commonly used in the calculation.

Since the problem is restricted to SAWs that have a wavevector in the x_1 direction, the solution is homogeneous in the direction x_2 and the calculation can be restricted to the x_1x_3 plane.

Translational symmetry in the x_1 -direction, enforced by the boundary conditions, implies degeneracy in case of resonant solutions. This undesirable degeneracy can be removed by placing one partial node of the steady wave into a domain corner with an additional constraint:

$$\mathbf{u}_3(1, x_2, 0) = 0. \quad (5.5)$$

The displacement field of such domain is then discretized with polynomial functions:

$$u_i = \sum_{k=0}^N \sqrt{2}\alpha_{ki}P_k\left(\frac{2x_3}{d} - 1\right) \sin(2\pi x_1) + \sum_{k=0}^N \sqrt{2}\beta_{ki}P_k\left(\frac{2x_3}{d} - 1\right) \cos(2\pi x_1), \quad (5.6)$$

where $x_1[0, 1]$, $x_3[0, d]$, P_k is a normalised Legendre polynomial of the k -th order, and α_{ki} and β_{ki} are coefficients of the approximation. When the function (5.6) is substituted back into equation for the Lagrangian energy (5.2), which is further integrated in terms of harmonic functions and Legendre polynomials, the (5.2) takes a new form:

$$\Lambda(\boldsymbol{\alpha}) = \frac{1}{2}\omega^2\boldsymbol{\alpha}^T\mathbf{M}\boldsymbol{\alpha} - \frac{1}{2}\boldsymbol{\alpha}^T\mathbf{K}\boldsymbol{\alpha}, \quad (5.7)$$

where $\boldsymbol{\alpha}$ is a column vector of coefficients α_{ki} and β_{ki} . A linear condition on the coefficients $\boldsymbol{\alpha}$ expresses the constraints defined on the computation domain:

$$\mathbf{C}\boldsymbol{\alpha} = 0. \quad (5.8)$$

Matrix \mathbf{M} is an identity matrix multiplied by the material density ρ , and matrix \mathbf{K} is symmetric and positive semi-definite, with components linearly dependent on c_{ijkl} .

Finally, the condition on Lagrangian's gradient:

$$\mathbf{0} = \nabla_{\boldsymbol{\alpha}}\Lambda(\boldsymbol{\alpha}) = (\omega^2\mathbf{M} - \mathbf{K})\boldsymbol{\alpha} \quad (5.9)$$

solved as an eigenvalue problem, leads to stationary points of the Langrange energy 5.7, i.e. bulk and surfaces resonances.

For each solution, ω represents the resonant frequency and can be recalculated to corresponding velocity as $v = \omega/2\pi$. The eigenvector $\boldsymbol{\alpha}$ represents the modal shape of the calculated mode, given as coefficient of the functional basis of discretized displacement field 5.6. This allows to recalculate the

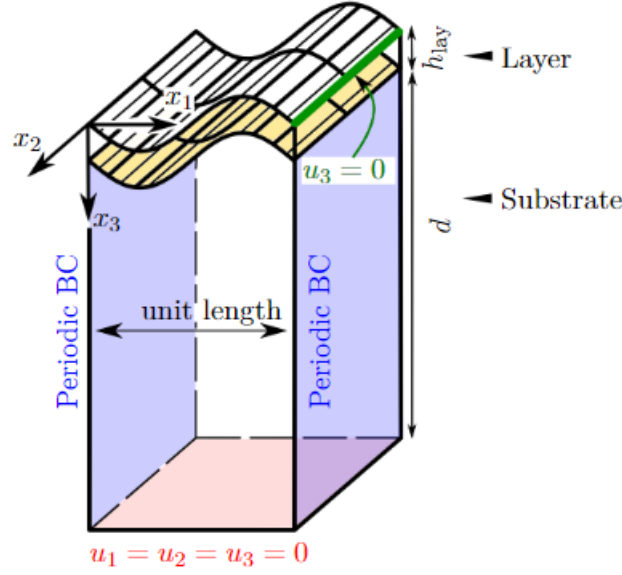


Figure 5.2: Computational domain for the film-substrate system with boundary conditions; taken from [43]

modal shape of each calculated mode and characterize its corresponding wavetype.

■ 5.1.1 Calculation for the supported layer

The Ritz-Rayleigh forward method can be used to solve the wave velocities in the layer-substrate system in a similar manner, as described in [44].

Main change is in the computational domain, see Fig. 5.2. The modified domain consists of two sub-domains, one for the layer and one for the substrate. Considering that the layers are of different materials and therefore of different elastic constants, the constraints are influenced as well:

- the functional basis remains the same, but each sub-domain has its own discretization
- periodic condition (5.3) and the condition on the domain base (5.4) remains unchanged
- the degeneracy-removing condition (5.5) is moved to the top of the layer domain
- and a new condition is set for the strain compatibility between the layer and substrate:

$$\mathbf{u}^{\text{lay}}(x_1, x_2, h_{\text{lay}}) = \mathbf{u}^{\text{sub}}(x_1, x_2, h_{\text{lay}}), \quad (5.10)$$

where h_{lay} is the height of the layer domain.

Due to these changes, the equation for the Lagrange energy 5.2 changes slightly, but the principles remain the same. The resulting eigenvector α is then constructed from parts corresponding to both subdomains. For more details, see [44].

5.2 The inverse problem

The elastic constants of material are determined by minimising the mismatch between the computed and experimentally measured SAW velocity data sets. It is reached by employing the inverse procedure, which executes iterative repetitions of the forward problem solution and consists of three stages:

First, the forward problem, fed with a set of guessed elastic constants, provides data set of wave velocities for all measured directions and wavemodes.

Second, an objective function is calculated – the objective function is defined as:

$$F(\mathbf{c}) = \sum_p \left(v_p^{\text{cal}}(\mathbf{c}) - v_p^{\text{exp}} \right)^2, \quad (5.11)$$

where c_j is a set of independent elastic constants, the superscript *cal* refers to calculated values and the superscript *exp* refers to experimental values.

And third, a new set of elastic constants is determined by a gradient-minimization approach.

The minimization problem runs iteratively, until a sufficient minimum of the objective function is found, i.e., the agreement of corresponding calculated and experimentally measured wave modes is satisfactory.

To characterize the error of the inverse-determined elastic constants, the Hessian approximation of the objective function can be used [42, 45] as:

$$\sigma_j = \sqrt{\sum_i \left(\alpha_j^i \right)^2 \frac{2F(c_j^{\text{min}})}{N\lambda_i}}, \quad (5.12)$$

where α_i and λ_i denote respectively the normalised i-th eigenvector and the corresponding eigenvalue of the Hessian matrix $d^2F/d(c_i)d(c_j)$ calculated in the minimum of F , and N is the number of fitted velocities. More details on the inverse procedure can be found in [42], or specifically for the supported-layer calculation in [44].

Chapter 6

Characterization of NiTi thin films

6.1 Samples

Thin epitaxial NiTi films deposited on MgO substrate were provided by colleagues Klara Lünser and Sebastian Fähler from Helmholtz-Zentrum Dresden-Rossendorf. Their basic characterisation is described in the Tab. 6.1 and Fig. 6.1.

sample name	film thickness (μm)	M_s ($^{\circ}\text{C}$)	M_f ($^{\circ}\text{C}$)	A_s ($^{\circ}\text{C}$)	A_f ($^{\circ}\text{C}$)	substrate
NiTi3100	3100 \pm 50	52.85	22.85	53.85	93.85	MgO
NiTi1680	1680 \pm 30	39.85	-0.15	16.85	72.85	MgO
NiTi1080	1080 \pm 80	40.85	7.85	30.85	82.85	MgO

Table 6.1: NiTi thin films properties

The characteristic temperatures of phase transformations were measured in a Physical Property Measurement System (PPMS) with four-point resistivity at a heating/cooling rate of 3 K/min and consequently recalculated to Celsius degree. R-phase reportedly does not occur in the samples.

Microstructures of the thin films at room temperature, composed of various martensitic variants, are illustrated in Fig. 6.1. Generally, the higher the thickness of the film, the more robust the variant domains. Given the epitaxial conditions, the single-crystalline austenite at elevated temperatures grows in 45° mismatch with respect to the substrate lattice. As the substrate is (001) plane, so is the austenite. However, the $[100]$ ¹ direction of the MgO substrate corresponds to $[110]$ direction of the austenite.

¹All directions are in Miller indices.

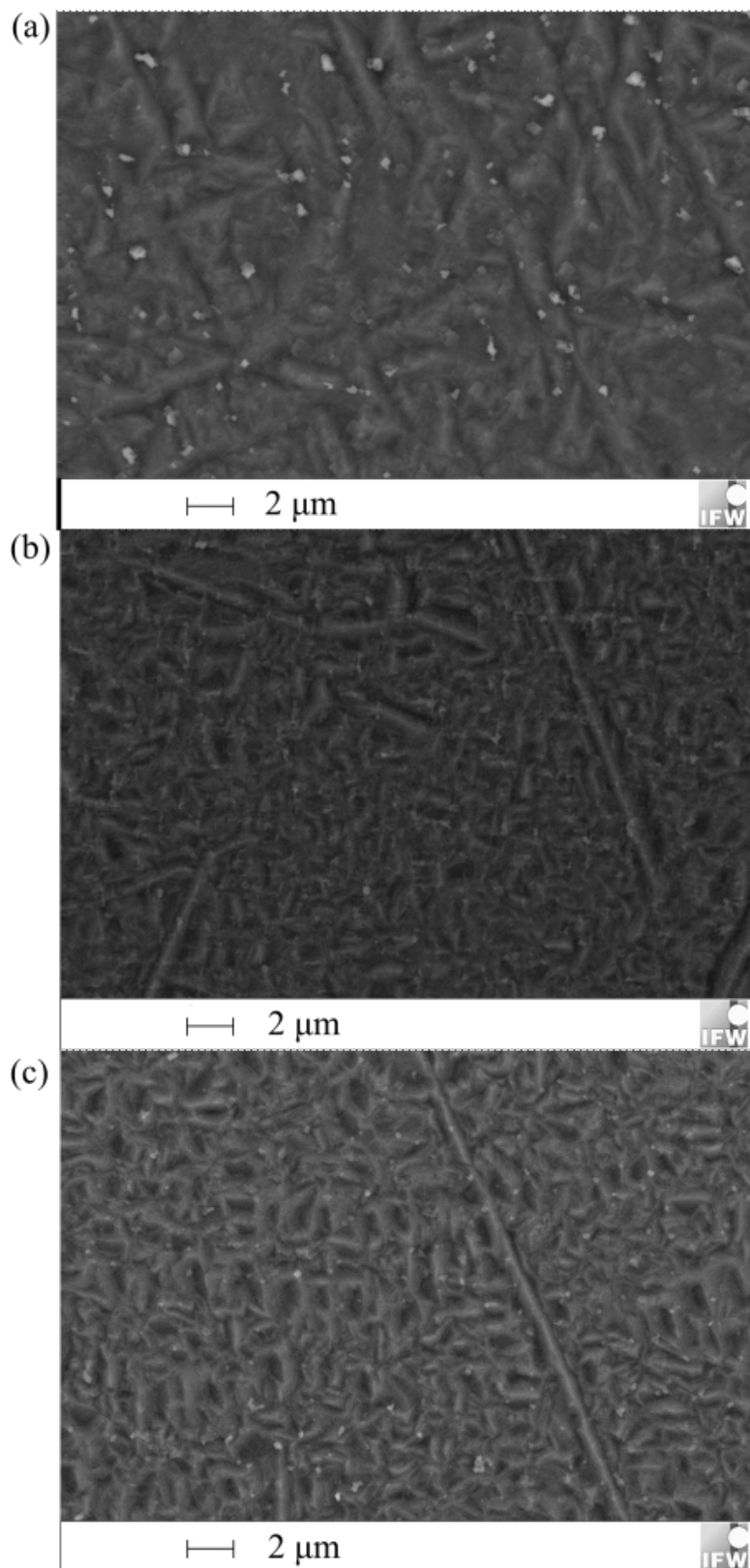


Figure 6.1: SEM pictures of the martensitic microstructures at room temperature for the samples: (a) NiTi3100, (b) NiTi1680, (c) NiTi1080, provided by K. Lünser

6.2 TGS of thermally cycled NiTi thin film sample

In order to verify the presence of the martensitic transformation in the supplied samples and consequently correctness of the critical temperature values as stated in Tab. 6.1, thermal cycling was carried out for one of the thin films, NiTi3100, in the range of 111 °C - 5 °C - 111 °C. However, the minimum temperature of 5 °C, i.e., well below M_f , was reached to complete the martensitic transformation without stabilisation. Therefore, the TGS measurement was obtained only at room and elevated temperatures of the range of 22 °C - 111 °C.

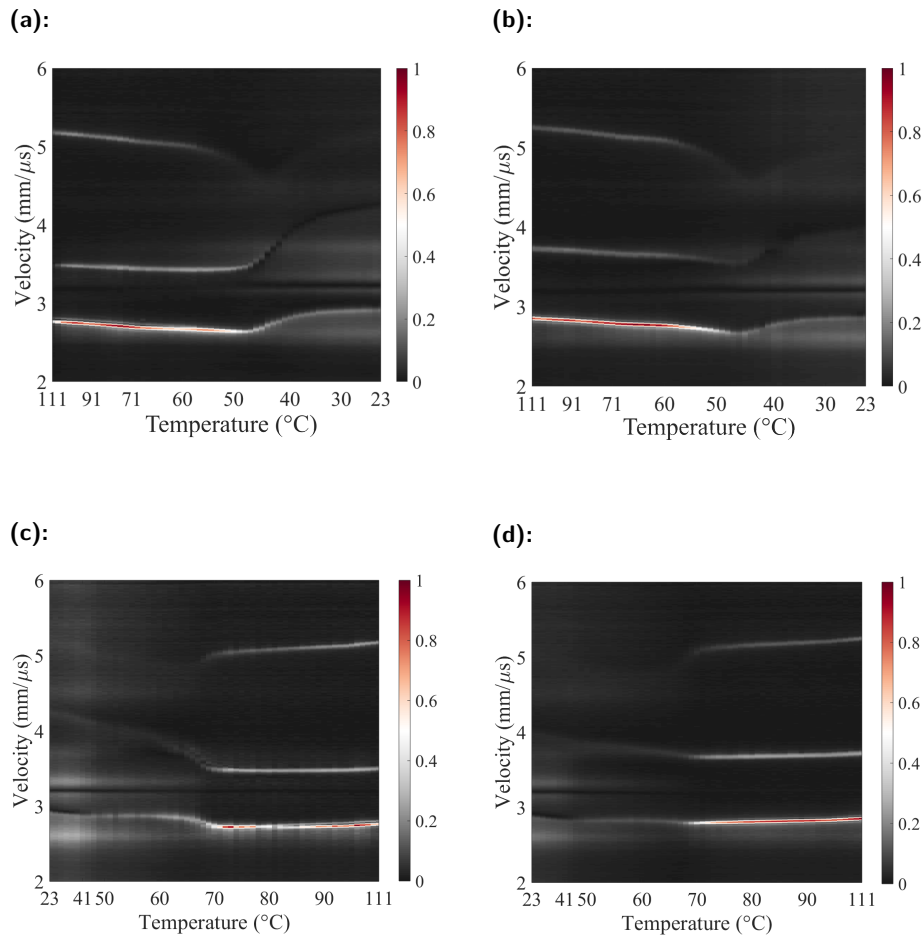


Figure 6.2: Thermal velocity maps of thermally cycled NiTi3100 at 10 μm at two various angles relative to the MgO substrate: (a) cooling at direction of [110], (b) cooling at direction of [100], (c) heating at direction of [110], (d) heating at direction of [100].

The velocity maps related to temperature as depicted in Fig. 6.2 show for both measured directions, [100] and [110] relative to the MgO substrate, three vibration modes. For all of them, the signal intensity gets reduced

when NiTi3100 transforms from austenitic into martensitic phase. Since identification of the critical temperatures of the transformation would not be precise if based on the velocity maps, only the most intense signal from each velocity map, i.e. the slowest mode, depicted in Fig. 6.2 was redrawn to provide hysteretic curves for both measured directions, see Fig. 6.3.

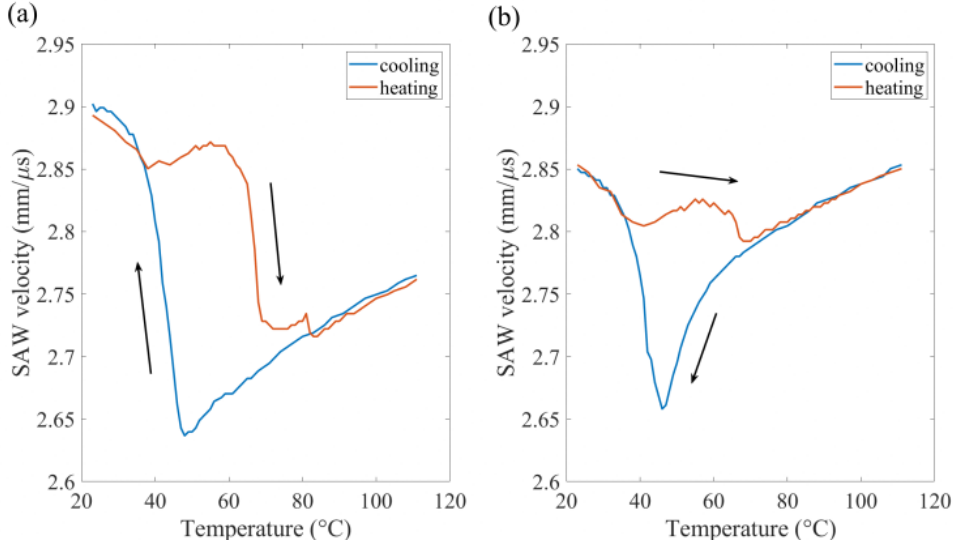


Figure 6.3: Thermal hysteresis of the SAW velocity dependent on temperature in NiTi 3100 measured relative to the MgO substrate at directions: (a) [110], (b) [100]

The hysteresis depicts one thermal cycle measured in the range of 111 °C – 22 °C – 111 °C for directions [100] and [110] relative to the MgO substrate. Based on that, the critical temperatures were approximated as $A_s \approx 60$ °C, $A_f \approx 80$ °C, $M_s \approx 45$ °C, $M_f \approx 24$ °C, which is in a relative agreement with the characteristic temperatures obtained with the resistivity method in Tab. 6.1. Nevertheless, the behaviour varies for heating and cooling curves. The cooling curve shows that the velocity decreases when cooling down to the temperature M_s , which corresponds with the phonon softening when nearing to the martensitic transformation [46, 47]. When the transformation begins, the material hardens again (the velocity increases). On the heating curve the material first softens as well, then a bump occurs and then hardens again. The bump indicates a presence of small percentage of R-phase which was not detected by the PPMS measurement.

The characteristic spiky feature on the heating curve at ~ 80 °C in Fig. 2.2a occurs as a consequence of the intersection of Rayleigh-type and TH-type waves as discussed below.

■ Angular measurement at room and elevated temperatures

Because only the strongest signal from velocity maps in Fig. 6.2 was utilized and the hysteresis curves are different for the two measured directions, measurements with angular rotation were conducted at two temperatures: at

111 °C and at room temperature. The angular velocity maps in Fig 6.4 show that the signals in Fig. 6.2 develop regularly with angle, confirming that there are higher-order wave modes detected, which can be used for elasticity characterization. For austenite at 111 °C, up to five modes were observed and for martensite at RT four modes, see Fig. 6.4a, b, respectively. To characterize the modes, Ritz-Rayleigh numerical method was applied; details are described in the chapter 5.

An intersection of the transverse-horizontal and Rayleigh waves occurs in austenite in [110]_MgO direction, which creates the spiky feature observed in thermal evolution of the Rayleigh wave peak in Fig. 6.3a.

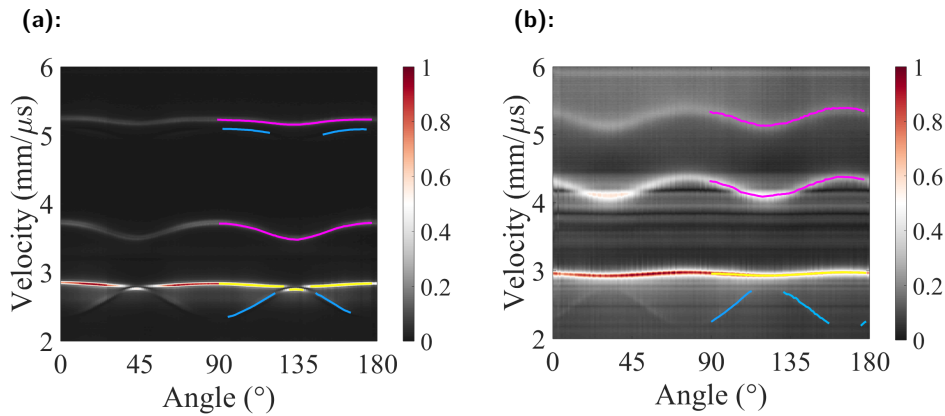


Figure 6.4: Angular velocity maps measured by TGS for NiTi 3100 at 10 μm at: (a) 111 °C, i.e., in austenite, and (b) room temperature, i.e., in martensite. The angle 0° corresponds to [100]_MgO direction. Blue colour indicates transverse-horizontal wave, yellow Rayleigh-type wave and magenta Sezawa wave.

6.2.1 Ritz-Rayleigh calculation for the NiTi thin films

Due to the high number of detected wave modes in the measurement with elevated temperature, it was possible to use the numerical inversion method, see section 5.2, to gradually improve the guess on elastic constants of the thin film by sequential association of detected signals and calculated modes. From the strongest measured signal to the lowest, see Fig. 6.4, the modes were characterized as the Rayleigh-type SAW (with most pronounced out-of-plane displacement), two Sezawa modes (with higher velocity due to more pronounced longitudinal displacement), and even first and second order transverse horizontal modes. These can be seen in directions out of principal axes, where they exhibit a slight out-of-plane displacement, allowing them to be detected by TGS.

Thus, the full elasticity matrix of the NiTi thin film in austenite at 111 °C can be provided:

$$c_{\alpha\beta} = \begin{pmatrix} 185.4 & 152.4 & 152.4 & 0 & 0 & 0 \\ 152.4 & 185.4 & 152.4 & 0 & 0 & 0 \\ 152.4 & 152.4 & 185.4 & 0 & 0 & 0 \\ 0 & 0 & 0 & 34.0 & 0 & 0 \\ 0 & 0 & 0 & 0 & 34.0 & 0 \\ 0 & 0 & 0 & 0 & 0 & 34.0 \end{pmatrix} \quad (6.1)$$

The resulting values of the elastic constants are in agreement with the values determined by ab initio calculations [48, 49]. The resulting Zener anisotropy ratio² of the single-crystalline austenite is approximately 2.

Since a microstructure forms with cooling to martensite, the surface quality is lower than for austenite, and one of the modes (the second-order transverse horizontal mode) cannot be found in the measured spectra.

Moreover, since the substrate-film interface clearly influences the microstructure, see Fig. 6.1, lower symmetry of the martensite can be expected - therefore, tetragonal elasticity was assumed for the inversion method. Note that a certain degree of caution is necessary for the inversion, more details in [44].

The resulting matrix obtained for martensite is:

$$c_{\alpha\beta} = \begin{pmatrix} 193.8 & 116.9 & 118.0 & 0 & 0 & 0 \\ 116.9 & 193.8 & 116.9 & 0 & 0 & 0 \\ 118.0 & 116.9 & 195.3 & 0 & 0 & 0 \\ 0 & 0 & 0 & 17.8 & 0 & 0 \\ 0 & 0 & 0 & 0 & 17.8 & 0 \\ 0 & 0 & 0 & 0 & 0 & 20.3 \end{pmatrix} \quad (6.2)$$

Since the expected accuracy of shear constants c_{44} and c_{66} is around 0.1 GPa [42], the difference of 2.5 shown in the elasticity matrix is a clear evidence of the effective tetragonality of the martensitic microstructure.

Interestingly, the degree of anisotropy remains quite high in martensite, with the generalized Zener ratio³ at 2.1 even slightly exceeding that of the austenite. This is unexpected, considering that austenite is a single crystal, while martensite possesses microstructure composed of various variants, and deserves a thorough exploration in the future.

6.3 TGS of NiTi thin films of various thicknesses

To characterize the samples and martensitic microstructures formed in the NiTi thin films of various thicknesses, see Fig. 6.1, the angular distribution of TGS was measured for other samples. However, as shown in following figures, the lower number of wave modes was detected for the other samples

²Zener anisotropy ratio $A = 2c_{44}/(c_{11} - c_{12})$

³Zener ratio generalized for non-cubic lattices is defined as the ratio of the highest and lowest velocity of the quasi-transverse wave mode.

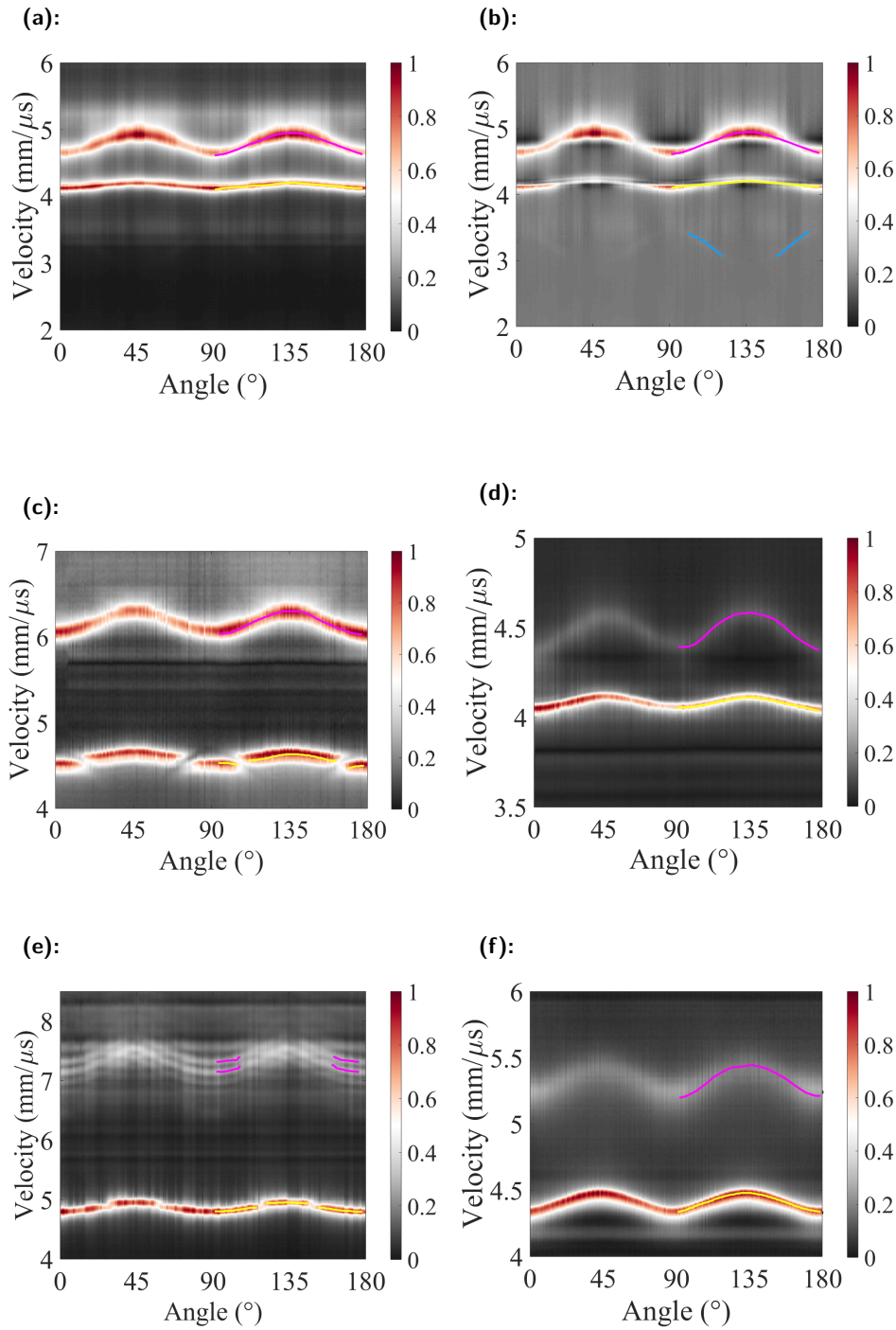


Figure 6.5: Angular velocity maps at room temperature: (a) NiTi3100 at 20 μm (raw signal), (b) NiTi3100 at 20 μm (median subtracted from the background), (c) NiTi1680 at 20 μm , (d) NiTi1680 at 10 μm , (e) NiTi1080 at 20 μm , (f) NiTi1080 at 10 μm , where blue colour indicates transverse-horizontal wave, yellow Rayleigh-type wave and magenta Sezawa wave. The angle 0° corresponds to [100]MgO direction.

than NiTi3100 since the low thicknesses prevent the propagation of higher modes in the films. Thus, since additional information can be obtained by frequency dispersion measurements with at least two various diffraction gratings/wavelengths, measurements with the $10\ \mu\text{m}$ acoustic wavelength were complemented by measurements with other wavelength of $20\ \mu\text{m}$. Although it would be beneficial to add a lower wavelength as well, the $5\ \mu\text{m}$ measurements showed high noise and added no significant information about the films - the results of these measurements were thus omitted in this work.

While not necessary to characterize the film, NiTi3100 measurement with $20\ \mu\text{m}$ was performed for information about expected results and calibration with known results. The results are shown in Fig. 6.5a, where the slower visible mode with velocity of $\approx 4\ \text{mm}/\mu\text{s}$ demonstrates a Rayleigh character while the faster one with velocity of $\approx 4.7\ \text{mm}/\mu\text{s}$ is Sezawa mode. Only after background correction by median subtraction the very weak signal of TH wave is observed, see Fig. 6.5b.

In the velocity maps of NiTi1680 measured with $20\ \mu\text{m}$, there are two wave modes observed, one with velocity of $\approx 4.5\ \text{mm}/\mu\text{s}$ and one with velocity of $\approx 6\ \text{mm}/\mu\text{s}$, see Fig. 6.5c. However, a closer look at the slower velocity mode reveals the presence of periodic discontinuities in the plot line. Such discontinuities indicate wave-mode intersection. In this case, it is the Rayleigh to pseudo-Rayleigh transition due to intersection with TH mode, see Fig. 3.7b, which allows for identification of the TH mode velocity at least at these points (as it remains hidden in other angles). The higher mode of velocity $\approx 6\ \text{mm}/\mu\text{s}$ is Sezawa mode, with more pronounced longitudinal character.

Velocity map of NiTi1680 at $10\ \mu\text{m}$ depicts two modes with velocities of $\approx 4\ \text{mm}/\mu\text{s}$ and $\approx 4.5\ \text{mm}/\mu\text{s}$, see Fig. 6.5d. The slower mode is again the Rayleigh-type mode, with a pronounced out-of-plane displacement leading to the strongest signal. The faster mode (Sezawa) has far lower amplitude and more pronounced anisotropy, suggesting a slightly different character of displacement, possibly more lateral character.

NiTi1080 at $20\ \mu\text{m}$ supports seemingly two waves modes with velocities of $\approx 4.9\ \text{mm}/\mu\text{s}$ and $\approx 7.3\ \text{mm}/\mu\text{s}$, see Fig. 6.5e. The higher intensity of the lower mode indicates a Rayleigh character. The regularly located points of lower intensity in the signal remind of points of intersection with TH mode; however, it cannot be observed in any other way than these intersections and is thus speculative. Two lines of the higher mode with stronger lateral character, i.e. less intense, suggest a split Sezawa mode, however this is also a hypothesis since their velocity is above that of the bulk qT wave in the substrate, and thus these modes would be supersonic in terms of the substrate-film system, see [30].

Velocity map of NiTi1080 at $10\ \mu\text{m}$ depicts two wave modes, see Fig. 6.5f. The lower mode with a velocity of $\approx 4.3\ \text{mm}/\mu\text{s}$ is a Rayleigh-type mode, while the higher mode of $\approx 5.2\ \text{mm}/\mu\text{s}$ has more lateral character.

Generally, a maximum number of wave modes can be detected when the film thickness is suitably large in relation to the wavelength used. Based on a comparison of the three thin film samples measured at the two wavelengths,

such a suitable ratio was reached for NiTi3100 at a wavelength of $10\ \mu\text{m}$, which provided information on the angle dispersion of the highest number of wave modes. A lower wavelength might excite further wave modes; moreover, the suitable ratio of film thickness and acoustic wavelength shows a linear dependence. Therefore, for a film with half the thickness, half the wavelength is required to observe a similar behavior - which explains the similarity of the velocity maps of NiTi3100 at $20\ \mu\text{m}$ and NiTi 1680 at $10\ \mu\text{m}$. Unfortunately, the measurement with $5\ \mu\text{m}$ wavelength was not sensitive enough and high noise in the velocity maps was observed. Thus, this remains a task for the future research.

Nevertheless, the measurement of two wavelengths for each film provided more information and wave modes to be studied. However, the inverse characterization of the film's elasticity of all samples is beyond scope of this work.

Chapter 7

Conclusion

Elastic waves with frequencies of hundreds of MHz were excited and detected by the transient grating spectroscopy in a contactless and thanks to the dominant thermoelastic regime also non-destructive way. The obtained frequency spectra of elastic waves propagating in the measured samples were converted into so called velocity maps which provide information about signal magnitude and its evolution with angle or temperature. Based on that information, Ritz-Rayleigh calculations were executed in order to determine the sample elasticity.

Three epitaxial thin films of NiTi - NiTi3100, NiTi1680 and NiTi1080, where the number indicates the film thickness in nanometers, were investigated. NiTi is an alloy exhibiting martensitic phase transformation which follows such a set of rules that it can be reversible and therefore leads to shape-memory effect. The epitaxial thin films are advantageous since the low thickness is related to faster response to temperature change compared to bulk material and the epitaxial nature may enable determination of martensite unit cell elasticity which is unknown to date.

Thermal cycling of NiTi3100 was performed in the range of 5 °C to 111 °C. Obtained hysteresis curves confirmed the martensitic nature of the phase transition and directional dependence and suggested presence of small percentage of R-phase which is in contradiction with the PPMS measurement. Due to the directional dependence, angular dispersion with wavelength of 10 μm was measured for austenite at 111 °C and martensite at room temperature and five wave modes in austenite and four wave modes in martensite were observed. Based on that, the elasticity constants for both phases were calculated by the Ritz-Rayleigh method. Austenite remains cubic even as an epitaxial film, while the martensitic microstructure is strongly affected by the interface with the substrate - leading to both dependence on the film thickness (with thicker films forming thicker variants) and surprisingly strong elastic anisotropy (even slightly exceeding that of the austenite).

Angular dispersion was measured as well for NiTi1680 and NiTi1080. Since the thicknesses of the films were insufficient for the propagation of higher modes, frequency dispersion measurements with two various wavelengths, 20 μm and 10 μm (5 μm was not sensitive enough), were performed to obtain additional information. However, further elasticity calculations are beyond

scope of this work.

Based on comparison of angular dispersion measured for all the three samples, it was demonstrated that the film thickness to wavelength ratio providing information about the highest number of wave modes is reached for the NiTi3100 film at 10 μm . Consequently, elasticity of the NiTi3100 film can be determined by the Ritz-Rayleigh numerical method from a single velocity map of this dispersion, unlike in case of the thinner films. Moreover, similarity of velocity maps of NiTi3100 at 20 μm and NiTi1680 at 10 μm is in agreement with the linear dependence of the suitable ratio of film thickness and acoustic wavelength.

In the further research, the explanation for the atypically high anisotropy of martensite should be searched for. Also, it would be suitable to subject the two thinner samples to surface Brillouin spectroscopy to substitute for the lower number of wave modes available by TGS so that elasticity could be reliably determined.



Bibliography

- [1] Carlotti, G. Elastic Characterization of Transparent and Opaque Films, Multilayers and Acoustic Resonators by Surface Brillouin Scattering: A Review. *Applied Sciences* **2018**, *8* (1), 124. <https://doi.org/10.3390/app8010124>
- [2] Every, A.; Maznev, A.; Grill, W.; et al. Bulk and surface acoustic wave phenomena in crystals: Observation and interpretation. *Bulk and surface acoustic wave phenomena in crystals: Observation and interpretation* **2013**, *50* (8), 1197–1217. <https://doi.org/10.1016/j.wavemoti.2013.02.007>
- [3] Wayman, C.; Duerig, T. An Introduction to Martensite and Shape Memory. *Engineering Aspects of Shape Memory Alloys*, 1st ed.; Butterworth-Heinemann Ltd, 1990; pp 3–20.
- [4] Yamauchi, K., Ohkata, I., Tsuchiya, K., Miyazaki, S., Eds. *Shape memory and superelastic alloys*, 1st ed.; Woodhead Publishing Limited, 2011.
- [5] Concilio, A. Historical background and future perspectives. *Shape Memory Alloy Engineering For Aerospace, Structural, and Biomedical Applications*, 2nd ed.; Butterworth-Heinemann, 2021; Chapter 1, pp 3–52.
- [6] Bhattacharya, K. Martensitic Phase Transformation. *Microstructure of Martensite: Why it forms and how it gives rise to the shape-memory effect*; Oxford University Press, 2004; Chapter 4, pp 46–65.
- [7] Wang, B.; Zhu, S. Seismic behavior of self-centering reinforced concrete wall enabled by superelastic shape memory alloy bars. *Bulletin of Earthquake Engineering* **2017**, *16* (1), 479–502. <https://doi.org/10.1007/s10518-017-0213-8>
- [8] Vishnu, K.; Strachan, A. Phase stability and transformations in NiTi from density functional theory calculations. *Acta Materialia* **2010**, *58*, 745–752. DOI:10.1016/J.ACTAMAT.2009.09.019
- [9] Buehler, W.; Gilfrich, J.; Wiley, R. Effect of Low-Temperature Phase Changes on the Mechanical Properties of Alloys near Composition TiNi. *Journal of Applied Physics* **1963**, *34* (5), 1475–1477. <https://doi.org/10.1063/1.1729603>

- [10] Mehta, K. Introduction. *Fabrication and Processing of Shape Memory Alloys*; Springer, 2019; Chapter 1, pp 1–7.
- [11] Miyazaki, S.; Otsuka, K. Development of Shape Memory Alloys. *ISIJ International* **1989**, *29* (5), 353–377. <https://doi.org/10.2355/isijinternational.29.353>
- [12] Miyazaki, S.; Otsuka, K. Mechanical behaviour associated with the premartensitic rhombohedral-phase transition in a Ti50Ni47Fe3 alloy. *Philosophical Magazine A* **1985**, *50* (3), 393–408. doi:10.1080/01418618408244235
- [13] Miyazaki, S.; Otsuka, K. Deformation and transition behavior associated with the R-phase in Ti-Ni alloys. *Metall Mater Trans A* **1986**, *17*, 53–63. <https://doi.org/10.1007/BF02644442>
- [14] Stachowiak, G.; McCormick, P. Shape memory behaviour associated with the R and martensitic transformations in a NiTi alloy. *Acta Metallurgica* **1988**, *36* (2), 291–297. [https://doi.org/10.1016/0001-6160\(88\)90006-5](https://doi.org/10.1016/0001-6160(88)90006-5)
- [15] Lexcelent, Ch. *Shape-memory Alloys Handbook*, 1st ed.; Wiley, 2013.
- [16] Miyazaki, S.; Kimura, S.; Otsuka, K.; Suzuki, Y. The habit plane and transformation strains associated with the martensitic transformation in Ti-Ni single crystals. *Scripta Metallurgica* **1984**, *18* (9), 883–888. [https://doi.org/10.1016/0036-9748\(84\)90254-0](https://doi.org/10.1016/0036-9748(84)90254-0)
- [17] Miyazaki, S.; Igo, Y.; Otsuka, K. Effect of thermal cycling on the transformation temperatures of Ti-Ni alloys. *Acta Metallurgica* **1986**, *34* (10), 2045–2051. [https://doi.org/10.1016/0001-6160\(86\)90263-4](https://doi.org/10.1016/0001-6160(86)90263-4)
- [18] Miyazaki, S.; Wayman, C. The R-phase transition and associated shape memory mechanism in Ti-Ni single crystals. *Acta Metallurgica* **1988**, *36* (1), 181–192. [https://doi.org/10.1016/0001-6160\(88\)90037-5](https://doi.org/10.1016/0001-6160(88)90037-5)
- [19] Miyazaki, S.; Otsuka, K.; Suzuki, Y. Transformation pseudoelasticity and deformation behavior in a Ti-50.6at%Ni alloy. *Scripta Metallurgica* **1981**, *15* (3), 287–292. [https://doi.org/10.1016/0036-9748\(81\)90346-X](https://doi.org/10.1016/0036-9748(81)90346-X)
- [20] Kudoh, Y.; Tokonami, M.; Miyazaki, S.; Otsuka, K. Crystal structure of the martensite in Ti-49.2 at.%Ni alloy analyzed by the single crystal X-ray diffraction method. *Acta Metallurgica* **1985**, *33* (11), 2049–2056. [https://doi.org/10.1016/0001-6160\(85\)90128-2](https://doi.org/10.1016/0001-6160(85)90128-2)
- [21] Tang, W. Thermodynamic study of the low-temperature phase B19(apostrof) and the martensitic transformation in near-equiatomic Ti-Ni shape memory alloys. *Metallurgical and Materials Transactions A* **1997**, *28* (3), 537–544. doi:10.1007/s11661-997-0041-6

- [22] Tan, S.M.; Miyazaki, S. Ti-content and annealing temperature dependence of deformation characteristics of TiXNi(92-X)Cu8 shape memory alloys. *Acta Materialia* **1998**, *46* (8), 2729–2740. [https://doi.org/10.1016/S1359-6454\(97\)00479-5](https://doi.org/10.1016/S1359-6454(97)00479-5)
- [23] Miyazaki, S. Thermal and Stress Cycling Effects and Fatigue Properties of Ni-Ti Alloys. *Engineering Aspects of Shape Memory Alloys*; 1st ed.; Butterworth-Heinemann Ltd., 1990; pp 394–413.
- [24] Winzek, B.; Schmitz, S.; Rumpf, H.; Sterzl, T.; et al. Recent developments in shape memory thin film technology. *Materials Science and Engineering: A* **2004**, *378* (1-2), 40–46. <https://doi.org/10.1016/j.msea.2003.09.105>
- [25] Walker, J.A.; Gabriel, K.J.; Mehregany, M. Thin film processing of shape memory alloy. *Sensors and Actuators* **1990**, *A21-A23*, 243–246.
- [26] Ishida, A.; Sato, M.; Takei, A.; Miyazaki, S. Effect of Heat Treatment on Shape Memory Behavior of Ti-rich Ti–Ni Thin Films. *Materials Transactions, JIM* **1995**, *36* (11), 1349–1355. <https://doi.org/10.2320/matertrans1989.36.1349>
- [27] Kajiwara, S.; Kikuchi, T.; Ogawa, K.; Matsunaga, T.; Miyazaki, S. Strengthening of Ti-Ni shape-memory films by coherent subnanometric plate precipitates. *Philosophical Magazine Letters* **1996**, *74* (3), 137–144. <https://doi.org/10.1080/095008396180281>
- [28] Miyazaki, S.; Ishida, A. Martensitic transformation and shape memory behavior in sputter-deposited TiNi-base thin films. *Materials Science and Engineering: A* **1999**, *273-275*, 106–133. [https://doi.org/10.1016/S0921-5093\(99\)00292-0](https://doi.org/10.1016/S0921-5093(99)00292-0)
- [29] Royer, D.; Dieulesaint, E. *Elastic Waves in Solids I, Free and Guided Propagation*; Springer, 2000.
- [30] Every, A.G. Measurement of the near-surface elastic properties of solids and thin supported films. *Measurement Science and Technology* **2002**, *13* (5), R21–R39. DOI 10.1088/0957-0233/13/5/201
- [31] Wolfe, J. P. Phonon focusing. *Imaging Phonons: Acoustic Wave Propagation in Solids*; Cambridge University Press, 1998; Chapter 2, pp 21–59.
- [32] Tiersten, H.F. Elastic Surface Waves Guided by Thin Films *Journal of Applied Physics* **1969**, *40* (2), 770–789. <https://doi.org/10.1063/1.1657463>
- [33] Wittkowski, T., Distler, G., Jung, K., Hillebrands, B., Comins, J. D. General methods for the determination of the stiffness tensor and mass density of thin films using Brillouin light scattering: Study of tungsten carbide films *Physical Review B* **2004**, *69* (20), 124. DOI:<https://doi.org/10.1103/PhysRevB.69.205401>

- [34] Royer, D.; Dieulesaint, E. Photothermal Generation. *Elastic Waves in Solids II, Generation, Acousto-optic Interaction, Applications*; Springer, 2000; Chapter 3.3, pp 210–225.
- [35] Grabec, T.; Sedlák, P.; Stoklasová, P.; Thomasová, M.; et al. In situ characterization of local elastic properties of thin shape memory films by surface acoustic waves. *Smart Materials and Structures* **2016**, *25* (12), 127002. DOI 10.1088/0964-1726/25/12/127002
- [36] Stoklasová, P.; Grabec, T.; Zoubková, K.; et al. Laser-Ultrasonic Characterization of Strongly Anisotropic Materials by Transient Grating Spectroscopy. *Experimental Mechanics* **2021**, *61* (4), 663–676. doi:10.1007/s11340-021-00698-6
- [37] Johnson, J.A.; Maznev, A.A.; Bulsara, M.T. Phase-controlled, heterodyne laser-induced transient grating measurements of thermal transport properties in opaque material. *Journal of Applied Physics* **2012**, *111* (2), 023503. <https://doi.org/10.1063/1.3675467>
- [38] Dennett, C.A.; Short, M.P. Thermal diffusivity determination using heterodyne phase insensitive transient grating spectroscopy. *Journal of Applied Physics* **2018**, *123* (21), 215109. <https://doi.org/10.1063/1.5026429>
- [39] Verstraeten, B.; Sermeus, J.; Salenbien, R.; ; et al. Determination of thermoelastic material properties by differential heterodyne detection of impulsive stimulated thermal scattering. *Photoacoustics* **2015**, *3* (2), 64–77. <https://doi.org/10.1016/j.pacs.2015.05.001>
- [40] Lim, T.C.; Farnell, G.W. Search for Forbidden Directions of Elastic Surface-Wave Propagation in Anisotropic Crystals. *Journal of Applied Physics* **1968**, *39* (9), 4319–4325. <https://doi.org/10.1063/1.1656967>
- [41] Every, A.G.; Kim, K.Y.; Maznev, A.A. The elastodynamic response of a semi-infinite anisotropic solid to sudden surface loading. *Journal of the Acoustical Society of America* **1997**, *102* (3), 1346–1355. <https://doi.org/10.1121/1.420053>
- [42] Stoklasová, P.; Sedlák, P.; Seiner, H.; Landa, M. Forward and inverse problems for surface acoustic waves in anisotropic media: A Ritz–Rayleigh method based approach. *Ultrasonics* **2015**, *56*, 381–389. <https://doi.org/10.1016/j.ultras.2014.09.004>
- [43] Grabec, T. Characterization of Complex Media by Surface Acoustic Waves utilizing Laser-Ultrasound Methods. Master Thesis, Czech Technical University in Prague, January 2017.
- [44] Grabec, T.; Soudná, Z.; Lünser, K.; Zoubková, K.; Stoklasová, P.; Sedlák, P.; Fähler, S.; Seiner, H. Characterizing elasticity of NiTi epitaxial thin film by transient grating spectroscopy. Submitted to *Journal of Sound and Vibration*

- [45] Janovská, M.; Sedlák, P.; Seiner, H.; Landa, M.; et al. Anisotropic elasticity of DyScO₃ substrates. *Journal of Physics: Condensed Matter* **2012**, *24* (38), 385404. doi:10.1088/0953-8984/24/38/385404
- [46] Ren X.A.; Otsuka K.A. The Role of Softening in Elastic Constant c_{44} in Martensitic Transformation *Scripta Materialia* **1998**, *38* (11), 1669–1675. [https://doi.org/10.1016/S1359-6462\(98\)00078-5](https://doi.org/10.1016/S1359-6462(98)00078-5)
- [47] Seiner H.; Kopeček J.; Sedlák P. et al. Microstructure, martensitic transformation and anomalies in c-softening in Co–Ni–Al ferromagnetic shape memory alloys *Acta Materialia* **2013**, *61* (15), 5869–5876. <https://doi.org/10.1016/j.actamat.2013.06.035>
- [48] Wagner, M. F.-X.; Windl, W. Lattice stability, elastic constants and macroscopic moduli of NiTi martensites from first principles *Acta Materialia* **2008**, *56* (20), 6232–6245. <https://doi.org/10.1016/j.actamat.2008.08.043>
- [49] Haskins, J. B.; Lawson, J. W. Finite temperature properties of NiTi from first principles simulations: Structure, mechanics, and thermodynamics *Journal of Applied Physics* **2017**, *121* (20), 205103. <https://doi.org/10.1063/1.4983818>